



저작자표시-비영리-변경금지 2.0 대한민국

이용자는 아래의 조건을 따르는 경우에 한하여 자유롭게

- 이 저작물을 복제, 배포, 전송, 전시, 공연 및 방송할 수 있습니다.

다음과 같은 조건을 따라야 합니다:



저작자표시. 귀하는 원저작자를 표시하여야 합니다.



비영리. 귀하는 이 저작물을 영리 목적으로 이용할 수 없습니다.



변경금지. 귀하는 이 저작물을 개작, 변형 또는 가공할 수 없습니다.

- 귀하는, 이 저작물의 재이용이나 배포의 경우, 이 저작물에 적용된 이용허락조건을 명확하게 나타내어야 합니다.
- 저작권자로부터 별도의 허가를 받으면 이러한 조건들은 적용되지 않습니다.

저작권법에 따른 이용자의 권리는 위의 내용에 의하여 영향을 받지 않습니다.

이것은 [이용허락규약\(Legal Code\)](#)을 이해하기 쉽게 요약한 것입니다.

[Disclaimer](#)

공학박사 학위논문

Tailor-made alloy design of
Zr-based metallic glass
for net-shape processing

Net-shape 공정을 위한
Zr계 비정질 합금의 맞춤형 설계

2022년 8월

서울대학교 대학원

재료공학부

김 경 준

Tailor-made alloy design of Zr-based metallic
glass for net-shape processing

Net-shape 공정을 위한
Zr계 비정질 합금의 맞춤형 설계

지도교수 박 은 수

이 논문을 공학박사 학위논문으로 제출함

2022년 7월

서울대학교 대학원

재료공학부

김 경 준

김경준의 공학박사 학위논문을 인준함

2022년 6월

위 원 장 _____ 한 흥 남 _____ (인)

부위원장 _____ 박 은 수 _____ (인)

위 원 _____ 이 명 규 _____ (인)

위 원 _____ 김 진 우 _____ (인)

위 원 _____ 류 옥 하 _____ (인)

Abstract

Tailor-made alloy design of Zr-based metallic glass for net-shape processing

Kyungjun Kim

Department of Materials Science and Engineering

College of Engineering

Seoul National University

Metallic glasses (MGs) exhibit excellent mechanical properties, such as high strength and large elastic limit of about 2%, and are attracting attention as the next-generation structural materials with unique characteristics facilitating excellent casting and thermoplastic forming (TPF). To date, more than a thousand different micro-scale and bulk-scale MGs have been developed in various systems, and it is quite encouraging that although most of them remain at the lab scale level, the field of application is diversifying. However, in order to promote the commercialization of MGs, the price of the constituent elements should be considered, and it is preferable that harmful elements such as Be are excluded. In addition, it is necessary to develop an alloy composition optimized in a direction where

efficiency of manufacturing process can be increased. In this study, we established an alloy design methodology and developed the Zr-based MGs which is suitable for existing net-shape manufacturing process, TPF and die casting. For tailor-made alloy design for MGs, we first tend to basically understand the correlation between the composition and the property changes in MGs.

Elastic moduli of MGs suggest a global and macroscopic view of a stiffness, and reflect both the interatomic atomic bonding energy and connectivity. In particular, the moduli of MGs are the essential factor which are directly related to thermodynamic, kinetic, mechanical, and physical properties of MGs. It is assumed that the moduli of MGs are determined by deformation of its solvent-solvent bonding, where atomic bonding is relatively less stiff. Therefore, the properties of MGs are determined by their atomic bonding between solvent atoms and are considered inherited from the properties of solvent element.

To investigate property changes in Zr-based metallic glass, we produced the ribbon alloys of Zr-TM (= Cu, Ni, Co, Fe) binary systems by melt-spinning, verified the glass phase formation by X-ray Diffraction (XRD) and high energy X-ray Scattering (XRS), and measured the characteristic temperature by Differential Scanning Calorimetry (DSC). In this study, it is confirmed that the tendency of characteristic temperature, such as glass transition temperature (T_g) and crystallization temperature (T_x), to be determined according to the Zr content in all four Zr-TM (= Cu, Ni, Co, Fe) binary alloy

systems. It can be considered that MG may have a lower T_g value in a composition with a higher Zr content. If it is practically possible, the T_g of pure Zr amorphous alloy may have a value similar to 517K. Unlike the other three alloys with the highest Zr content in binary systems which exhibit typical thermal characteristics of a marginal MG, $Zr_{70}Cu_{30}$ MG shows a relatively wide super-cooled liquid region ($\Delta T_x = T_x - T_g$) of about 50K.

Based on this understanding, we found the novel Zr-based alloy with optimum property for being applied the TPF process and facilities for conventional plastics. Lowering glass transition temperature in Zr-based MG is basically limited because of high stability of the beta-Zr phase. The alloy composition of $Zr_{70}Cu_{16}Ni_4Co_4Al_6$, which has the lower T_g of 625 K compared to the conventional Zr-based MGs for TPF, large thermoforming window (i.e. over 70K with heating rate 40K/min), and excellent TPFA in Zr-based MG, was systematically designed. The thermoforming window, and TPFA depending on the various heating rate were measured by DSC and Flash-DSC. We concluded that the developed MG in this study can be sufficient candidate for utilizing both processes and facilities for advanced engineering plastics such as PBI and PI. In consideration of GFA, mechanical properties, and TPFA with heating rate, it is expected that the forming process for a small-size product, such as micro- and nano-scale films or fibers, is suitable for the developed alloy.

We also provided an alloy design methodology suitable for near-net-shape manufacturing through suction casting while considering GFA, hardness, and fluidity. Hardness, GFA, and fluidity are sensitively dependent on the alloy composition in Zr-based bulk metallic glass (BMG)-forming alloys. Generally, GFA and fluidity are trade-off characteristics each other, because strong glass formers have high viscosity in the liquid state, and fluidity decreases. However, GFA and fluidity can be ensured at the same time through alloy design around the near-eutectic compositions. We utilized the liquidus projection of ZrCuNi ternary system, and it was possible to predict compositions with low T_1 close to the eutectic point in the ZrCuNiAl quaternary alloy system. In particular, it was efficient to replace Zr with Ag in order to increase hardness while simultaneously acquiring improvement of GFA and reduction of T_1 . Therefore, we developed $Zr_{50}Cu_{24}Ni_{10}Al_8Ag_8$ BMG that exhibits not only excellent GFA and hardness, also about a 40 % increase in flow length compared to that of Vit-106. This BMG has great potential for being high-value structural materials with complex shapes through near-net-shape casting.

In this study we found the alloy design not only that is optimized for being applied the TPF process and facilities for conventional plastics but also that is suitable for near-net-shape manufacturing with simultaneously excellent GFA, hardness, and fluidity. This study provides practical guide to promote to the commercialization of MG

by reducing the initial investment cost in the TPF process, and to tailor-made alloy design which allows BMG to be utilized in the various industrial part through various near-net-shape casting methods.

Keywords : Metallic glass, Bulk metallic glass, Thermoplastic forming, Thermoplastic window, Net-shape forming, Fluidity

Student Number : 2015 – 20799

Table of Contents

Abstract	i
Table of Contents	vi
List of Figures	x
List of Tables	xvi
Chapter 1. Introduction	1
1.1. Metallic glasses as advanced materials	1
1.2. Recent research trends	5
1.3. Structural applications	8
1.3.1. Advantages of metallic glass	8
1.3.2. Fabrication process of metallic glass	11
1.3.3. Commercial Zr-based metallic glass	13
1.4. Thesis motivation and objectives	15

Chapter 2. Experimental procedures	16
2.1. Sample preparation	16
2.1.1. Arc-melting	16
2.1.2. Melt-spinning	18
2.1.3. Suction casting	19
2.2. Structural analysis	20
2.2.1. X-ray diffraction	20
2.2.2. High energy X-ray scattering	20
2.3. Thermal analysis	22
2.3.1. Differential scanning calorimetry	22
2.3.2. Thermogravimetric Analyzer/differential scanning calorimetry	23
2.3.3. Flash DSC	23
2.4. Mechanical analysis	24
2.4.1. Micro hardness test	24
2.5. Fluidity test	25

Chapter 3. Fundamental understanding of property changes in Zr-based metallic glass	26
3.1. Properties inheritance in metallic glass	26
3.2. Modulus changes depending on base metal contents	27
3.3. Glass formation in Zr–TM binary metallic glass	32
3.4. Thermal property changes in Zr–TM binary metallic glass	34
Chapter 4. Development of Zr-based metallic glasses applicable to thermoplastic process and facilities of engineering plastics	37
4.1. Processing temperature for amorphous materials	40
4.2. Compositional dependence of thermal property	50
4.3. Thermal property optimization in Zr-based multicomponent system	52
4.4. Formability evaluation	58
4.5. Processing temperature map drawing	62

Chapter 5. Development of Zr-based bulk metallic glasses suitable for near-net-shape manufacturing	69
5.1. Process efficiency in net-shape manufacturing	69
5.2. Design of quaternary and quinary bulk metallic glass with low T_l	72
5.3. Hardness- T_g -Zr content correlation	80
5.4. GFA evaluation	82
5.5. Fluidity test	85
 Chapter 6. Conclusion	 91
 Bibliography	 I
 Abstract in Korean	 XXIV

List of Figures

Fig. 1.1. Volume change according to temperature change during solidification of liquid phase

Fig. 1.2. (a) Schematic illustration for structure of crystalline metal. (b) High-resolution TEM image of a low carbon steel measured in [111] direction. Inset image of the corresponding selected-area electron diffraction pattern which shows sharp spots, (Reprinted from [2] with permission provided by Springer Nature and Copyright Clearance Center) (c) Schematic illustration for structure of MG, (d) High-resolution TEM image of $Zr_{67}Ni_{33}$ metallic glass. Inset image of the corresponding selected-area electron diffraction pattern which shows diffuse halo pattern (Reprinted from [2] with permission provided by Springer Nature and Copyright Clearance Center)

Fig. 1.3. Schematic diagram for room temperature yield of metals, composites, and polymers or flexural strength of ceramics as a function of modulus. (Reprinted from [19] with permission provided by Elsevier and Copyright Clearance Center)

Fig. 2.1. The overview of arc-melting equipment and the detailed view of inside the arc-melting chamber.

Fig. 2.2. The overview of melt-spinning and the detailed view of inside the melt-spinning chamber.

Fig. 2.3. The illustration of setup layout for high resolution synchrotron XRS measurement, PLS-II 5A beam line in Pohang, Republic of Korea.

Fig. 3.1. Schematic illustration of the local atomic bonding strength between the clusters. (Reprinted from [56] with permission provided by AIP publishing and Copyright Clearance Center)

Fig. 3.2. Linear correlation of calculated modulus line and measured elastic modulus (Reprinted from [57] with permission provided by Elsevier and Copyright Clearance Center) according to composition change in Zr–Cu binary system

Fig. 3.3. Phase analysis by XRD and heat flow curves measurement by DSC of Zr–Cu, Zr–Ni, Zr–Co, and Zr–Fe binary MGs.

Fig. 3.4. Alloy compositions which can form metallic glass fabricated by melt–spinning in Zr–TM (= Cu, Ni, Co, and Fe) binary alloy systems and their characteristic temperature, T_g and T_x .

Fig. 3.5. (a) Linear correlation between T_g , T_x with Zr content in Zr–TM (= Cu, Ni, Co, and Fe) binary alloys. The blue line is the linear fitting of T_g in the Zr–TM (= Cu, Ni, Co, Fe) binary alloys. **(b)** Heat flow curves measured by DSC instruments of the composition with the highest Zr content in each alloy system.

Fig. 4.1. Schematic diagram of thermoformable amorphous pyramid according to the glass transition temperature, which shows comparison of amorphous polymer plastics and amorphous alloys

(metallic glasses). The higher the glass transition temperature, the better the performance, but the higher process cost.

Fig. 4.2. Strength and Young's modulus values of conventional amorphous polymer plastics and MGs, arranged according to the T_g . The mechanical properties of plastics and MGs which have similar values of T_g are compared.

Fig. 4.3. Schematic diagram for TPF process of metallic glass. (a) Illustration of thermoforming window of MG. Isochronal CHT curve, isothermal TTT curve and T_g curves are plotted. TPF is performed in the temperature range within T_g to T_x . Schematics of casting, TPF by conventional heating and ultra-fast heating are illustrated. (b) The schematic illustration of TPF process of MG after casting.

Fig. 4.4. T_g and ΔT_x of Zr-TM (= Cu, Ni, Co, Fe) binary alloys. Zr₇₀Cu₃₀ alloy shows potentially thermal property of thermoformable binary MG because of its low T_g and wide ΔT_x .

Fig. 4.5. Measurement of variations in T_g and ΔT_x of ternary alloys in ZrCuNi and ZrCuCo systems. (a) The compositions of ZrCuNi alloys fabricated by melt-spinning are plotted on the Zr-Cu-Ni liquidus projection. (b, c) XRD patterns and heat flow curves of ZrCuNi alloys represented according to increase of the Zr content from the Zr_{71.2}Cu₂₄Ni_{4.8} composition. (d, e) XRD patterns and heat flow curves of ZrCuNi alloys represented between Zr₇₀Cu₃₀ and Zr₇₆Ni₂₄. (f) The compositions of ZrCuCo alloys fabricated by melt-

spinning are expressed on the Zr–Cu–Co liquidus projection. **(g, h)** XRD patterns and heat flow curves of ZrCuCo alloys represented according to increase of the Zr content from the $Zr_{71.8}Cu_{24}Co_{4.2}$ composition. **(i, j)** XRD patterns and heat flow curves of ZrCuCo alloys represented between $Zr_{70}Cu_{30}$ and $Zr_{79}Co_{21}$.

Fig. 4.6. The value of T_g and ΔT_x of Zr–based MGs designed in binary to senior alloy systems. **(a)** T_g exhibits a linear correlation inversely proportional to Zr content, whereas ΔT_x changes greatly depending on the combination of additional alloying elements. **(b)** $Zr_{70}Cu_{16}Ni_4Co_4Al_6$ is selected as the representative composition in this study for thermoforming because of the low T_g and wide ΔT_x of 70 K.

Fig. 4.7. Comparison of the TPFAs between the MGs developed in this study and the previously reported BMGs through two different parameters, $\Delta T_F (= T_l - T_x)$, a TPFAs parameter which is possible to be evaluated simply by measuring T_l and T_x , and $(T_x^2 / m T) / (T_l - T_x)^2$, a TPFAs parameter considered as a factor in ideal condition. The fragility value, m , for some alloys is estimated.

Fig. 4.8. CHT curves and thermoforming windows of the 3 representative alloys developed in this study at various heating rates between 10^{-1} and 10^4 K/s, measured by Flash–DSC. The values of T_g , T_x and the fitted CHT curves for **(a)** $Zr_{76}Ni_{24}$, **(b)** $Zr_{70}Cu_{30}$, and **(c)** $Zr_{70}Cu_{14}Ni_4Co_4Al_6$ alloys. **(d)** Comparison of temperature–time thermoforming windows between T_g and T_x in CHT curves.

Fig. 4.9. The range of thermoforming window and TPFA parameter, $S = (T_x - T_g) / (T_l - T_g)$, of $Zr_{70}Cu_{14}Ni_4Co_4Al_6$ MG compared to T_g of conventional engineering plastics. The faster the heating rate, the wider the thermoforming temperature range and the better the TPFA.

Fig. 5.1. (a) Liquidus projection of ZrCuNi ternary systems and 10 at. % Al plane of ZrCuNiAl quaternary phase diagram. **(b)** Schematic illustration of the glass-forming region in a pseudo-binary phase diagram with an asymmetric eutectic-coupled zone.

Fig. 5.2. Phase analysis and thermal analysis of the Vit-106 and $Zr_{60-x}Cu_{16+2x}Ni_{14-x}Al_{10}$ ($x = 0, 2, 4, 6, 8$ at. %) BMGs. **(a)** X-ray diffraction patterns of the as-cast rod samples with 6 mm in diameter. **(b)** Heat flow curves showing characteristic temperatures of MG (T_g , T_x , and T_L). **(c)** Changes in T_g and T_x according to the Zr content. **(d)** Change in T_L according to the Zr content.

Fig. 5.3. Phase analysis and thermal analysis of the $(Zr_{60-x}Cu_{16+2x}Ni_{14-x}Al_{10})_{97}Nb_3$ ($x = 0, 2, 4, 6, 8$ at. %), and $Zr_{54-x}Cu_{16+2x}Ni_{14-x}Al_8Ag_8$ ($x = 0, 4, 8$ at. %) BMGs. **(a)** X-ray diffraction patterns of the as-cast rod samples with 6 mm in diameter. **(b)** Heat flow curves showing characteristic temperatures of MG (T_g , T_x , and T_L). **(c)** Changes in T_g and T_x according to the Zr content. **(d)** Change in T_L according to the Zr content.

Fig. 5.4. 3-dimensional plot of (T_g) –(Vickers hardness)–(Zr

content) of the Zr-based BMGs developed in this study. Three projections (T_g - Zr content / T_g - Hardness / Hardness - Zr content) and their linear fitted lines are arranged on each axial plane.

Fig. 5.5. (a) T_L - Zr content, and ϵ - Zr content plots of the Zr-based BMGs developed in this study. **(b)** Z_{max} - ϵ plots of the Vit-106, three selected alloys with lowest T_L and highest ϵ for each alloy system, ZrCuNiAl, ZrCuNiAlNb, and ZrCuNiAlAg, of **Fig. 5.5. (a)**, and other previously reported BMGs of various alloy systems.

Fig. 5.6. Flow length measurement by suction casting. **(a)** A schematic illustration of the suction casting equipment for measuring the flow length of BMGs in this study. **(b)** An image showing that a BMG sample drawn into the 1 mm diameter passage of the Cu mold by suction. **(c)** Flow length - T_L plot of Vit-106 and the selected alloys with the lowest T_L for the three alloy systems ZrCuNiAl, ZrCuNiAlNb, and ZrCuNiAlAg, respectively. The inset image exhibits the representative samples of each alloy composition for the fluidity test.

List of Tables

Table 1.1. Summary of BMGs with critical size over 10mm [17]

Table 4.1. T_g , tensile strength and Young's modulus of representative amorphous plastics [94–98]

Table 4.2. T_g , compressive strength and Young's modulus of MGs [99–100]

Table 4.3. MGs of various alloy systems and the ΔT_F values for TPFA comparison.

Chapter 1.

Introduction

1.1. Metallic glasses as advanced materials

Generally, molten metal is crystallized at the melting temperature (T_m) with slow cooling. If the cooling rate is increased, metal in liquid state does not crystallize even at the melting temperature (T_m) but maintains the super-cooled liquid state. As the degree of undercooling increases, the driving force for nucleation increases, but mobility of atoms is rapidly reduced and nucleation is hindered. Therefore, when metal in liquid state is cooled to a low temperature at a critical cooling rate, mutual movement of atoms is impossible and the liquid structure is sustained. Then it does not transform into crystals and solidifies homogeneously, this vitrified metal is called metallic glass (MG). The temperature at which molten metal is vitrified is considered to be the point at which viscosity of the liquid becomes 10^{12} Pa · s, this temperature is referred to the glass transition temperature (T_g)

Fig. 1.1. shows the volume change according to the temperature change during solidification of liquid phase. As shown in figure, metal in liquid state undergoes a sudden change in volume at T_m during the

crystallization process. During vitrification process, only slope of the volume change varies through the super-cooled liquid state, and the temperature at which the slope change occurs is the same as T_g . At this temperature, the alloy finally solidifies into a frozen-in liquid atomic structure. [1]

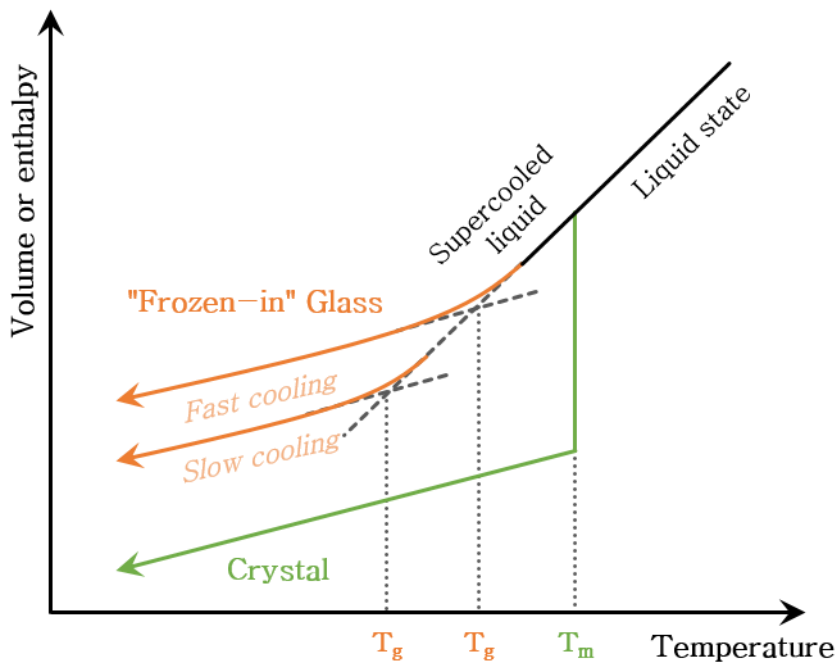


Fig. 1.1. Volume change according to temperature change during solidification of liquid phase

As shown in schematic illustration in **Fig 1.2. (a)**, most of metallic materials are arrays of crystals. Each atom in these materials has a long-range translational periodicity in 3D and is located in the crystal

lattice. In **Fig. 1.2. (b)**, it is indicated that high-resolution TEM image of a low carbon steel measured in $[111]$ direction and inset image of the corresponding selected-area electron diffraction pattern which shows sharp spots. On the other hand, amorphous alloys with a frozen-in liquid structure through quenching have a disordered structure similar to a liquid state as described in **Fig. 1.2. (c)**. In **Fig. 1.2. (d)**, it is suggested that high-resolution TEM image of $Zr_{67}Ni_{33}$ metallic glass and inset image of the corresponding selected-area electron diffraction pattern which shows diffuse halo patterns.

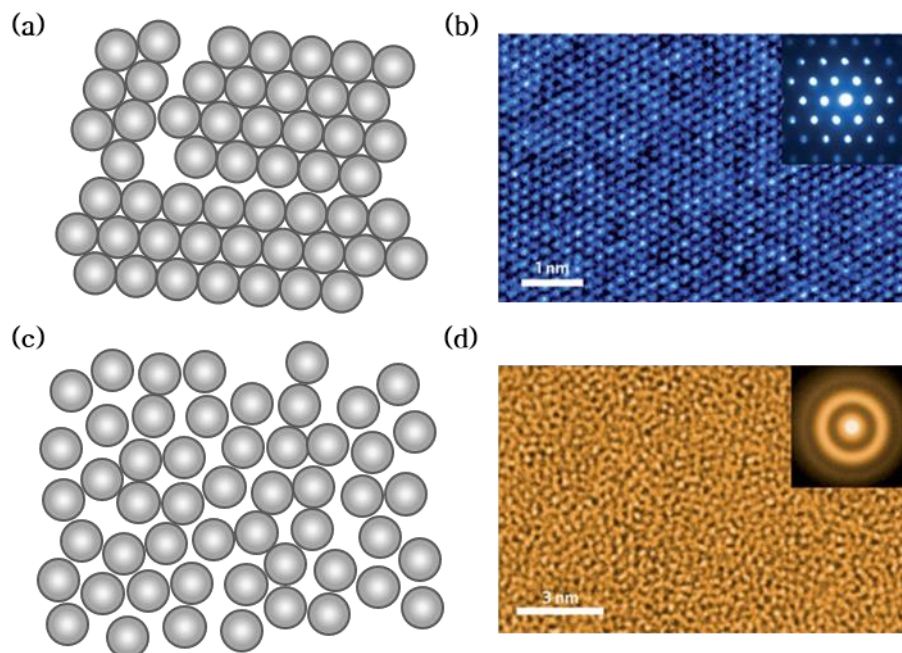


Fig. 1.2. (a) Schematic illustration for structure of crystalline metal. (b) High-resolution TEM image of a low carbon steel measured in $[111]$ direction. Inset image of the corresponding selected-area

electron diffraction pattern which shows sharp spots, (Reprinted from [2] with permission through Springer Nature and Copyright Clearance Center) (c) Schematic illustration for structure of MG, (d) High-resolution TEM image of $Zr_{67}Ni_{33}$ metallic glass. Inset image of the corresponding selected-area electron diffraction pattern which shows diffuse halo pattern (Reprinted from [2] with permission through Springer Nature and Copyright Clearance Center)

MGs have unique characteristics different from the structural properties of crystalline metal, such as grain boundary or defect. Due to these structural characteristics, MGs have excellent mechanical property, such as high strength, large elastic limit of about 2% and high resilience, and exhibits outstanding chemical resistance. As promising materials applied for a wide range of applications, MGs are considered as high-level structural materials and preferred over conventional materials such as metals, ceramics, magnetics due to their remarkable properties.

1.2. Recent research trends

Before to the 1960s, some of non-crystalline metallic materials were produced by condensation process with metallic element vapor on substrates. [3] In 1960, W. Klement, R.H. Willens, and P. Duwez at California Institute of Technology first reported the synthesis of an amorphous alloy, $\text{Au}_{75}\text{Si}_{25}$, by rapid quenching. [4] To restrain crystallization which limits the critical size of sample to micro-scale, a high cooling rate around 10^6 K/s was required. The importance of this study was that more types of alloys could be synthesized into the glassy state compared to the vapor condensation process. In the 1960s, H.S. Chen and D. Turnbull developed various Pd-based MGs such as Pd-Si-Ag, Pd-Si-Cu, and Pd-Si-Au with a cooling rates of 10^3 K/s. This allowed the fabrication of fully amorphous alloys with critical thicknesses of 0.5 mm. [5-7] In 1974, H.S. Chen reported the fabrication of Pd-Cu-Si MG with a diameter up to 1 mm using a simple method, suction casting, which was regarded to be the first BMG. [8] Further investigations on other Pd-based BMG-forming alloys had been systematically conducted to obtain a critical casting diameter of 1-3 mm by quenching the melt, contained in a fused silica quartz tube, into water. In the early 1980s, D. Turnbull's research group reported the fabrication of $\text{Pd}_{40}\text{Ni}_{40}\text{P}_{20}$ BMG with diameters of 5mm. [9] In 1984, they enlarged the critical sample diameter up to 10 mm by quenching the Pd-Ni-P melt with boron oxide flux in fused

silica tube. [10] These studies attracted an amount of interest in both academic world and industrial field. However, due to the high cost of noble elements and severe processing condition, such as cooling rate and vacuum state, the sample size of glassy alloys was restricted to micro-scale thin sheets and wires, so that it was unlikely to find wide range of applications. From the late 1980s, A. Inoue's research group at Tohoku University developed many kinds of novel BMGs in diverse multi-component alloy systems with a critical cooling rate below 10^2 K/s and critical thickness over several centi-meter. This report from A. Inoue's research group demonstrated that formation of BMG is not limited to a few special alloy systems and feasible in various alloy systems than previous thought. [11–15] In 1992, A. Peker and W.L. Johnson at Caltech reported $Zr_{41.2}Cu_{12.5}Ni_{10}Ti_{13.8}Be_{22.5}$ BMG which shows a critical cooling rate of 1 K/s and critical diameter up to 10 cm. [16] This alloy is known as Vitreloy 1 or LM-1, the first commercial BMG. Starting from this Vitreloy1, diverse commercial Zr-based BMG series have been developed. For a few decades, the critical casting thickness of BMGs has been continuously enhanced by more than three orders of magnitude and more than a thousand different BMGs have been developed in Ln-, Mg-, Zr-, Pd-, Pt-, Fe-, Cu-, Ni- and Ti-based systems. In addition, various MGs with different elements and compositions have been investigated.

System	Alloy composition (at. %)	Critical size, D_c (mm)	Method	Year
Pd-based	$Pd_{40}Ni_{40}P_{20}$	10	Fluxing	1984
	$Pd_{40}Cu_{30}Ni_{10}P_{20}$	72	Water quenching	1997
Zr-based	$Zr_{65}Al_{7.5}Ni_{10}Cu_{17.5}$	16	Water quenching	1993
	$Zr_{41.5}Ti_{13.8}Cu_{12.5}Ni_{10}Be_{22.5}$	25	Copper mold casting	1996
Cu-based	$Cu_{40}Zr_{42}Al_7Y_5$	10	Copper mold casting	2004
	$Cu_{49}Hf_{42}Al_9$	10	Copper mold casting	2006
RE-based	$Y_{36}Sc_{20}Al_{24}Co_{20}$	25	Water quenching	2003
	$La_{62}Al_{15.7}Cu_{11.15}Ni_{11.15}$	11	Copper mold casting	2003
Mg-based	$Mg_{54}Cu_{26.5}Ag_{8.5}Gd_{11}$	25	Copper mold casting	2005
	$Mg_{65}Cu_{7.5}Ni_{7.5}Zn_5Ag_5Y_5Gd_5$	14	Copper mold casting	2005
Fe-based	$Fe_{48}Cr_{15}Mo_{14}Er_2C_{15}B_6$	12	Copper mold casting	2004
	$(Fe_{44.3}Cr_5Co_5Mo_{12.8}Mn_{11.2}C_{15.8}B_{5.9})_{98.5}Y_{1.5}$	12	Copper mold casting	2004
	$Fe_{41}Co_7Cr_{15}Mo_{14}C_{15}B_6Y_2$	16	Copper mold casting	2005
Co-based	$Co_{48}Cr_{15}M_{14}C_{15}B_6Er_2$	10	Copper mold casting	2006
Ti-based	$Ti_{40}Zr_{25}Cu_{12}Ni_3Be_{20}$	14	Copper mold casting	2005
Ca-based	$Ca_{65}Mg_{15}Zn_{20}$	15	Copper mold casting	2004
Pt-based	$Pt_{42.5}Cu_{27}Ni_{9.5}P_{21}$	20	Water quenching	2004

Table 1.1. Summary of BMGs with critical size over 10mm [17]

1.3. Structural Applications

1.3.1 Advantages of metallic glass

The failure behavior of crystalline metallic materials is dominantly determined by the function of the quantity, distribution as well as nature of dislocations, which is the defects in crystalline lattice. On the other hand, MGs show different failure behavior because their lack of both dislocations and slip planes. Consequently, they exhibit unique mechanical properties than crystalline metallic materials. [18] BMGs show extremely high strength and large elastic limit, meaning they are able to endure a large stress without permanent deformation before yielding. In fact, MGs exhibit strength close to theoretical maximum even than steels or Ti-alloys, which means they are the strongest materials among metals, composites, polymers and ceramics (see **Fig. 1.3.**). However, if the stress above the yield point is applied, they tend to fail catastrophically. When crystalline metallic materials are strained above the yield point, they exhibit strain hardening. Dislocations prefer to form at locations of shear enhanced zone. Materials are hardened by those dislocations locally assembled, and thereby shear relocate away from the original source. This redistribution of stress through the whole of the bulk-scale induce a relatively homogenous deformation. Because there is the absence of dislocation in BMGs, they tend to locally shear in narrow region, ~ 10

nm bands. The high shear rate produces heat that leads to the material in the narrow shear region to dilate and weaken, which lower the shear resistance and increase shear rate even more. Therefore, strain softening is accelerated and the material tends to fail catastrophically.

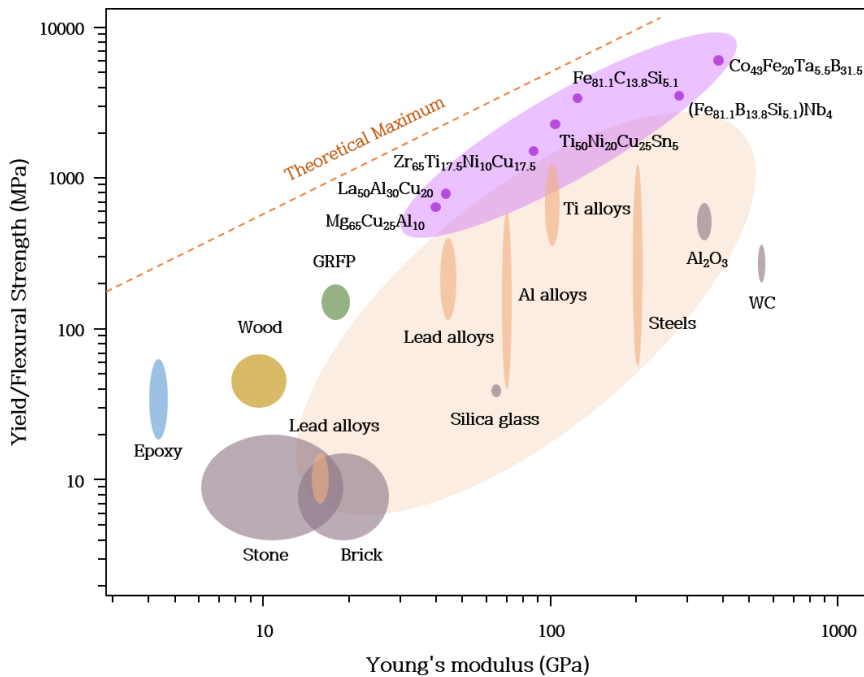


Fig. 1.3. Schematic diagram for room temperature yield of metals, composites, and polymers or flexural strength of ceramics as a function of modulus. (Reprinted from [19] with permission provided by Elsevier and Copyright Clearance Center)

Another important parameter of mechanical durability is toughness, which means resistance of materials against the propagation of cracks. MGs indicate large difference in property of toughness. Small cracks easily grow into large fractures in some brittle MGs. Whereas others are impressively tough. [20–22] It is possible that the difference has correlation with elastic stiffness of each material under strain and pressure condition. [23] MGs, which are more subject to shear than to pressure and have a low shear modulus compared to the bulk modulus, tend to be tougher. Under stress, shear bands are formed and propagated, which vanish the energy and lower the probability of a crack to form. However, recent evidence indicates that other factors, such as the cooling rate and processing conditions, also play an important role. [24] Also, ductility, the ability to plastically deform and bend without breaking, is another interest for MGs. Generally, MGs are ductile only when their thickness is less 10 times than the critical crack length. The critical crack is the length of the largest crack which the material can withstand before significant softening. Usually, the critical crack length is around 100 μm for most BMGs, so casting thicknesses under 1 mm is required to achieve bending ductility in BMGs. [25–27]

1.3.2. Processing of metallic glass

First, two types of fabrication processes, suction casting and die casting have been adopted for the net shape manufacturing of BMGs. Among these processes, a product with excellent quality, such as higher surface finish and lower porosity, can be realized with the suction casting rather than the die casting. Usually, BMGs with low melting temperature have benefit because they lower energy consumption, save tool cost by reducing thermal shock and fatigue, and shorten cycle time during net shape process. An overheating above threshold temperature rather than cooling rates greatly affects crystallization behavior, further the TTT diagram (Time–Temperature–Transformation diagram) and critical cooling rate. [28] GFA can shrink if the maximum temperature of liquid melt before cooling process doesn't go over the limit of a threshold temperature. Also, the overheating affects the liquid viscosity in most of BMGs. [29] Liquid viscosity variation phenomenon can be generally seen in the melting of an oxide phase and a chemical decomposition process. [30–31] During the casting processes of metallic products, both suction casting and die casting, shrinkage is a major consideration. However, the shrinkage phenomenon can be negligible in BMGs because there's the absence of a first order transition during solidification in BMGs. Cooling process in the fabrication plays an important role. Low solidification shrinkage in BMGs rarely causes a

gap between the mold and the BMG during the cooling process. [32–33] The heat transfer through the gap is respectively different whether it is under the condition of atmosphere or vacuum. Also, this can affect the cooling rate or even can be the limiting factor. In the direct casting process of BMGs, rapid cooling and forming should be done simultaneously due to its crystallization mechanism and phase transformation kinetics. [34–35] It must be carefully conducted when direct casting to prevent crystallization during mold filling and solidification. This process can be especially difficult while making a product with complicate surface.

TPF is the alternative fabrication process for MGs to direct casting. This process is occasionally called as the process hot forming, hot pressing, superplastic forming, viscous flow working and viscous flow forming. MGs exhibit unique softening behavior above their T_g and this softening phenomenon led to the study and development on TPF of MGs. The preferred condition for TPF is the extreme softening of the MGs during heating above T_g and their secured thermal stability. Thermal stability is main consideration for the measurement of ability for TPF to maintain an amorphous structure during heating above T_g . It can be also quantified by the degree of the super-cooled liquid region (SCLR). For $Zr_{44}Ti_{11}Cu_{10}Ni_{10}Be_{25}$, long processing time at low temperature is necessary because of its high viscosity. [36] At a high temperature, the viscosity is considerably reduced, so that processing time can be reduced.

Commonly, low viscosity and the long processing time in SCLR are the best condition for the optimum formability of MGs. It has been reported that thermos-physical properties for evaluating better formability of MGs are fragile liquid behavior, large poisson's ratio and low T_g . Processing temperature and pressure to implement the softening phenomenon above the T_g and in the SCLR is different for each MG applicable for TPF. [37] The capacity for plastic forming of MGs in the SCLR was recognized by researchers. Various processing methods based on the TPF are exploited, so that the enhanced thermoplastic formability of MGs attracts a wide range of researchers.

1.3.3. Commercial Zr-based metallic glass

W.L. Johnson and A. Peker at Caltech developed a novel BMG, $Zr_{41.2}Ti_{13.8}Cu_{12.5}Ni_{10.0}Be_{22.5}$, based on Zr-based alloy system in 1992, [38] as part of a US Department of Energy and NASA funding project for developing new aerospace materials. With critical casting thickness of up to 10 cm feasible in silica containers, this alloy was known as Vitreloy1 (Vit.1), the first commercial BMG. Subsequently, Vitreloy2 (Vit.2), $Zr_{46.75}Ti_{8.25}Cu_{7.5}Ni_{10}Be_{27.5}$, and other Vitreloy series have been developed. Recently, A.A. Kündig at ETH Zürich has been investigating Zr-Ti-Cu-Ni-Al BMGs, [39] focusing on their similar

alloy, Vit.105, $Zr_{52.5}Ti_5Cu_{17.9}Ni_{14.6}Al_{10}$, one of the best glass forming alloys. Vitreloy series contain a large number of different sized elements inducing to a free volume around 1% at the melting point, so that, they have high liquid viscosity. In the solid state, atoms are difficult to move past each other, resulting in high corrosion and wear resistance.

As mentioned above, MGs, especially Zr-based BMGs, have similar densities but high yield strength closed to theoretical strength around 1.9 GPa and large elastic limit around 2% compared to conventional steels and Ti-alloys. Therefore, MGs have high strength-to-weight ratio, making them possible to replace Al-alloys, but with more optimum resistance to permanent plastic deformation and fracture toughness simultaneously. Low damping nature by less absorption and greater release of energy causes the material to elastically restore to its original shape even under high stress and strain. This ability for shape memory enables the use of MGs in applications such as structural materials.

1.4. Thesis motivation and objectives

In the previous section, MGs, a promising metallic materials as future structural material, was introduced. Until now, various studies have been conducted to discuss the excellent properties of MGs, and it is quite encouraging that although most of them remain at the lab scale level, the field of application is diversifying. Research on the composition of MGs was generally conducted in the direction of finding an excellent GFA composition. Accordingly, research was mainly conducted on alloy systems containing noble metal elements such as Pt, Au, and Pd, or alloy systems containing harmful elements such as Be elements. In order to promote the commercialization of an amorphous alloy, it is necessary to not only consider the cost of alloying elements, but also exclude harmful elements. In addition, research needs to be conducted in the direction of finding an alloy composition that is suitable for the process of producing an alloy and can increase process efficiency. The objectives of this study is to find an alloy suitable for the TPF process utilizing the intrinsic characteristic temperature of an amorphous alloy, and an alloy suitable for die-casting, which is one of the net-shape processing commonly used in commercial alloys. Therefore, it is aimed to first investigate the correlation between the composition of MG and the change in properties, and to design a property-customized alloy suitable for TPF process and die-casting.

Chapter 2.

Experimental procedures

2.1. Sample preparation

2.1.1. Arc-melting

The mother alloy ingots were fabricated by arc-melting under a Ti-gettered argon atmosphere on a water-cooled copper hearth shown in **Fig. 2.1**. The mixtures of high purity elements (99.95% or 99.99%) for the specifically desired compositions of Zr-TM (= Cu, Ni, Co, Fe) system and Zr-TM (= Cu, Ni, Co, Fe, Nb, Ag) - Al system were prepared through weighing in 0.1mg-scale. The each weighed elements were put on a water-cooled copper hearth inside the chamber of arc-melting equipment (SAMHAN Vacuum Development Co. Ltd.). Then, the chamber was evacuated into a high-vacuum condition under $1.5 * 10^{-5}$ torr and was purged by high purity (99.999%) argon gas. Before melting the mixture of elements, the pure Ti-getter was melted, which act to absorb residual oxygen in a high purity argon atmosphere. The mixtures of elements were melted by arc plasma generated between a tungsten electrode and copper hearth. The alloy ingots were re-melted at least 4~5 times in order

to retain compositional homogeneity. Weight loss of alloy ingots after melting was limited less than 1% of the initial weight.

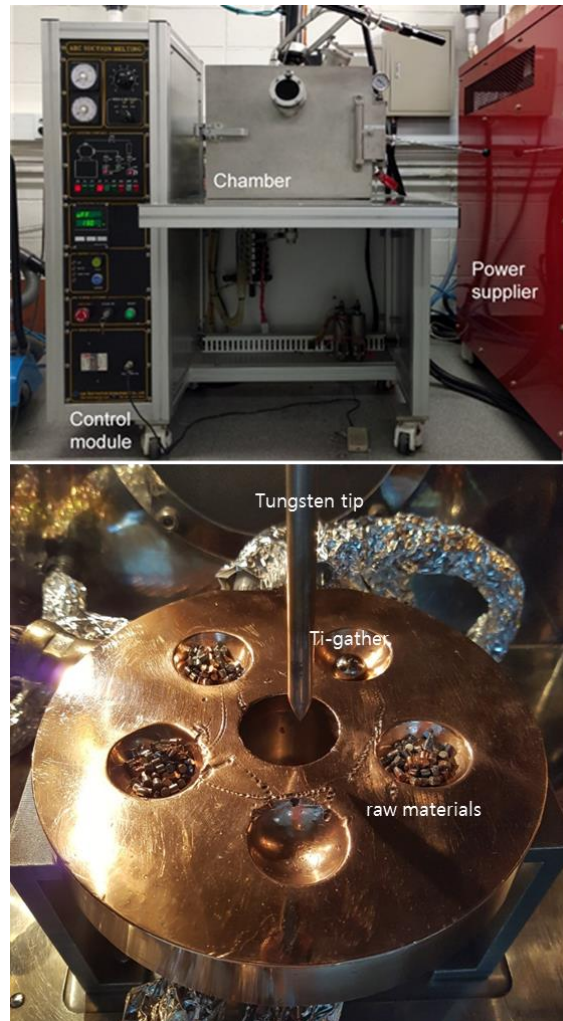


Fig. 2.1. The overview of arc-melting equipment and the detailed view of inside the arc-melting chamber.

2.1.2. Melt-spinning

Ribbon samples of Zr-TM (= Cu, Ni, Co, Fe) system and Zr-TM (= Cu, Ni, Co, Fe, Nb, Ag)-Al system were prepared by melt-spinning, one of rapid solidification process. The alloy ingots fabricated by arc-melting were placed in 10 mm inner diameter quartz tubes. The quartz tubes with 0.5 mm to 1 mm nozzle in the bottom were held inside the chamber of melt-spinning equipment (SAMHAN Vacuum Development Co. Ltd.). Then, a high vacuum condition of the chamber was set under $1.5 * 10^{-5}$ torr and was purged by high purity (99.999%) argon gas. The alloy ingots were re-melted by induction coil, and then ejected with pressure of 50 kPa through a quartz nozzle onto a copper wheel rotating with 3000RPM or over. The ribbon samples that was fabricated through this process had the thicknesses of $\sim 30 \mu\text{m}$ and the widths of ~ 2 mm.

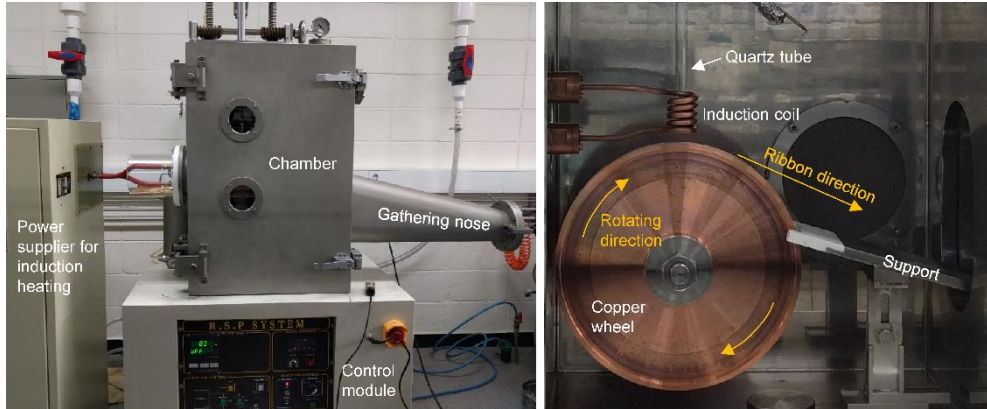


Fig. 2.2. The overview of melt-spinning and the detailed view of inside the melt-spinning chamber.

2.1.3. Suction casting

Cylindrical rod samples with 6mm diameter and 50 mm height of some Zr-TM (= Cu, Ni, Co, Fe, Nb, Ag)-Al system were prepared by re-melting alloy ingot through the suction casting apparatus. The suction casting apparatus was installed in the arc-melting equipment (SAMHAN Vacuum Development Co. Ltd.). For structural analysis and mechanical property test, the rod samples were cut by low speed cutter and high speed cutter after fabrication. Then, mechanical polishing was applied up to 1200 grit on the cutting surface. Weight loss by melting process was controlled to be less than 1% of the initial weight.

2.2. Structural analysis

2.2.1. X-ray diffraction

Structure of the ribbon samples and the bulk rod samples were analyzed by X-ray diffraction (XRD, Bruker D2 phaser and New D-8 advance) using monochromatic Cu K α radiation to identify its phase. The 2θ range is scanned within range from 20° to 80° with a scanning rate of 0.5 degree per second. For diffraction pattern on flat surface of the ribbon samples, the samples were placed on the plate glasses. Also, for diffraction pattern on mid-part of the bulk rod samples, the samples were cut and polished.

2.2.2. High energy X-ray scattering

For the high energy X-ray scattering analysis of as-spun Zr-Cu ribbons samples, room temperature high resolution synchrotron X-ray scattering (XRS) was conducted with ~ 17.9 keV energy and a wavelength $\lambda = 0.69265$ nm at the 5A beamline of Pohang Light Source (PLS-II in Pohang, Republic of Korea). The setup layout for this XRS measurement is illustrated in **Fig. 2.3** as a schematic diagram.

Ribbon samples were measured in transmission mode. The scanned range of the scattering angle, 2θ , in this analysis was typically from 4.4° to 175° , which corresponds to the range of the momentum transfer, $Q (=4\pi/\lambda)\sin\theta$, from 0 to 13\AA^{-1} .

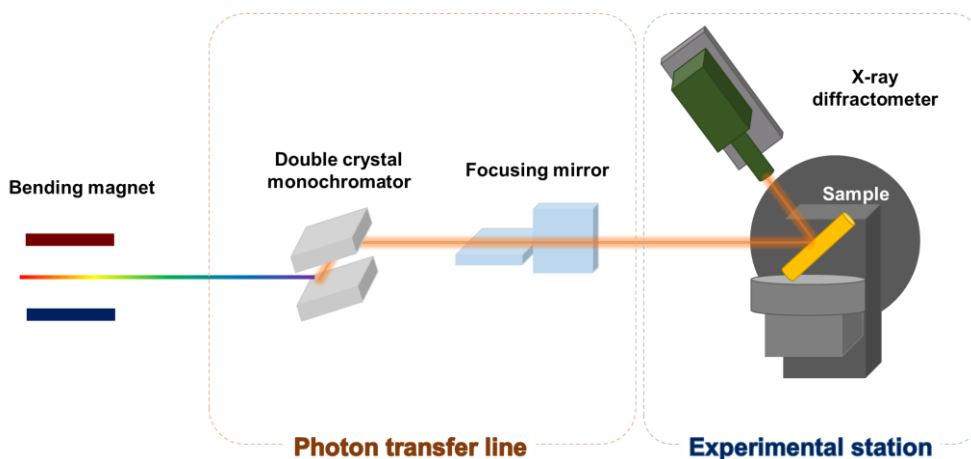


Fig. 2.3. The illustration of setup layout for high resolution synchrotron XRS measurement, PLS-II 5A beam line in Pohang, Republic of Korea.

2.3. Thermal analysis

2.3.1. Differential scanning calorimetry

The differential scanning calorimeter (Perkin Elmer DSC 8500) with intra-cooler system with an operating temperature range within 223 to 1023 K was utilized to measure heat flow signal, such as endothermic and exothermic, and to identify crystallization behavior of the prepared samples during heating scan, cooling scan and isothermal process. Small pieces of the ribbon samples were enclosed in Al or Cu pan for the measurement and an empty pan was utilized as a reference. Pt-based apparatus cell was purged with high purity (99.999%) argon gas with a flow rate of 20 ml/min to prevent sample oxidation. Before sample measurement, calibration of the equipment was conducted using high purity In and Zn standards. The temperature scan was measured with a heating rate from 10 K/min to 160 K/min, depending on samples. In isothermal measurement, the sample temperature was controlled to the preset temperature with a heating rate of 40 K/min and kept isothermally.

2.3.2. Thermogravimetric Analyzer/differential scanning calorimetry

To measure the heat flow curves, including T_g , T_x , and T_l , for some bulk rod samples of Zr–TM (= Cu, Ni, Co, Fe, Nb, Ag)–Al system, thermogravimetric analyzer/differential scanning calorimetry (TGA/DSC1, METTLER TOLEDO) were utilized in this study. Small pieces of the samples were enclosed alumina crucible. The heat flow curves were scanned from 273K to 1200K with a heating rate of 20 K/min. Before the experiment, heating procedures of several blank crucibles were performed to get the baseline for correction

2.3.3. Flash DSC

Fast differential scanning calorimeter, which is known as Flash DSC (Flash DSC 2+, Mettler Toledo) was utilized to measure isothermal and continuous thermal scanning for some ribbon samples of Zr–TM (= Cu, Ni, Co, Fe)–Al system at fast heating rates within 100 K/s to 10000 K/s. The ribbon samples were cut into the small pieces (smaller than 0.1 mm * 0.1 mm), and placed on the MultiSTAR UFS 1 MEMS chip sensors. A little drop of distilled water was applied with

the sample to attach the samples on the rough surface of chip sensors. Distilled water act as an adhesive between the sample and the surfaces of chip sensors. Droplet evaporates immediately before heating scan and does not damage thermal sensor or sample during heating scan.

2.4. Mechanical analysis

2.4.1. Micro hardness test

Vickers hardness for the bulk rod samples of Zr–TM (= Cu, Ni, Co, Fe, Nb, Ag)–Al system were evaluated by measurement of a micro hardness test equipment (EMCO–TEST DuraScan 70) under a loading of 0.1 kgf. Before hardness measurement, the samples were cut by low speed cutter and high speed cutter. Then, mechanical polishing was applied up to 1200 grit on the cutting surface for accurate measurement. The hardness tests were repeated ~20 times to obtain a mean values, and standard deviations between measured values were used as an error ranges.

2.5. Fluidity test

The fluidity for the bulk glass former of Zr-TM (= Cu, Ni, Co, Fe, Nb, Ag)-Al system was tested through a low-pressure suction casting at a pressure of 0.5 bar (Samhan Vacuum Development CO.LTD). For evaluation of flow lengths under equivalent conditions, the weight of the specimen of the BMG alloys was matched to 4.0 ± 0.1 g, the power current for melting was controlled to 200 A, and the temperature gradient inside the specimen was equalized for 1 minute of arc-plasma. The flow length was measured with the flow distance through the 1 mm diameter passage using the water-cooled copper mold.

Chapter 3.

Study for property of Zr–TM binary metallic glass

3.1. Properties inheritance in metallic glass

In contrast to the existing alloys, MGs have liquid-like disordered structure which is considered to inherit from their liquid state. [40–42] For fundamental understanding and ultimate controlling the mechanical, thermal properties of MGs, it is essential to establish their correlation with structural features. In a macroscopic way, MGs are regarded as isotropic and homogeneous. However, they have atomic-scale short range orders (SRO) and nano-scale medium range orders (MRO). In particular, the SRO of MGs is a structural inheritance of liquids. [40–44] The SRO of MGs are modeled by a small cluster which is composed centered solute atoms surrounded by multiple solvent atoms. Also, the nanoscale MRO is indicated by densely packed superclusters consisting of inter-connected clusters. [45–49] Both the two types of orders, SRO and MRO, have an effect on the structural features and properties of MGs, but are rarely hard to be distinguished. The nature of atoms packing inside MGs and the

role of the local ordering in mechanical and thermal properties remain a conundrum and draw attention. [40–49] So far, the understanding and the knowledge of amorphous structure are largely based on study of structural modeling and simulations. MGs macroscopically seems to inherit disordered structure from their liquid state, but in reality, they inherit atomic–scale and nano–scale structure, SRO and MRO, respectively. Recently, it was identified that Poisson's ratio of MGs is decided by the viscous characteristic from their liquid state. This demonstrated that the properties of MGs could be inherited from their liquid state. [50–52] Therefore, inheritances of the structural features from their liquid state in MGs can suggest a fundamental understanding and issues of their origin of mechanical, thermal properties.

3.2. Modulus changes depending on base metal contents

Among the metallic materials, MGs are the simplest materials consisting of atomic packing clusters, such as SRO and MRO, which interact each other. Elastic moduli generally suggest a global view of an internal stiffness which is related to interatomic bonding strength. Since MGs can be fabricated in both many kinds of alloy systems and

alloy compositions including multi-component, they have various types of atomic structures, resulting in a significant range of elastic properties. As a result, the elastic moduli of MGs determined by its constituent component and composition, act as easily measurable parameters and are the main physical parameters to control the kinetic, mechanical, physical, and thermodynamic properties of super-cooled liquids of metallic materials and MGs. Because the elastic moduli of MGs are considered to be associated with the structural features by the components, such as their macroscopic isotropy behavior and homogeneity, many studies have been investigated to recognize the correlation between structure and modulus. However, these research topics are still challenging due to the complexity of structural features in the MGs.

In general, the elastic moduli in metallic materials are considered to be the average of the moduli from each component, so called the "rule of mixture". The simple method, which is calculation of the average value from the moduli of each constituent element based on "rule of mixtures", was suggested. Considering that MGs are systematically consist of atomic packing cluster with constituent elements, the elastic moduli of MGs have been accepted as the weighted averages of those from their constituents based on the "rule of mixtures" in nature. [53–54] It is possible to calculate each in iso-stress condition and iso-strain condition as follows simplified equations.

$$1 / M = \sum (f_i * 1 / M_i)$$

and

$$M = \sum (f_i * M_i)$$

where M_i is the elastic modulus of constituent element and f_i is atomic percent of element. However, these theoretical prediction is difficult to be applied since the deformation of the MGs does not in practice occur in the iso-stress condition or iso-strain condition.

It has recently been investigated that the elastic moduli of MGs have correlation with their solvent element. Considering the atomic packing structure of MGs, solvent-solvent bonding between each cluster, in which bonding strength is relatively less stiff, is deformed. [55] Therefore, the elastic properties of MGs are mainly determined by the weakest atomic bonding between their solvent element. In addition, regarding the elastic properties in each alloy system, it was found that softening phenomenon varies depending on the amount of solvent element. [56] The phenomenon called universal softening is reported that the shear modulus varies linearly with the base metal content. Also, such a universal softening phenomenon is accompanied by the local fluctuations, both positive and negative, in atomic bond strength of MGs. **Fig. 3.1.** is schematic illustration of the local fluctuation in the atomic bonding strength including positive and negative, and that of crystalline base metal. **Fig. 3.2.** is a schematic illustration which describes calculated modulus of Zr-Cu binary MG

and extrapolated point indicating MG consisting of pure Cu and Zr, respectively. Solvent–solute transition composition is described in consideration of atomic radius difference between Zr and Cu. Also, elastic modulus measured by nano–indentation (Reprinted from [57] with permission provided by Elsevier and Copyright Clearance Center) is indicated, and it can be seen that the variation tendency between the calculated value and the measured value is approximately consistent. As mentioned above, it can be found that the modulus changes linearly according to the base element content from solvent–solute transition point.

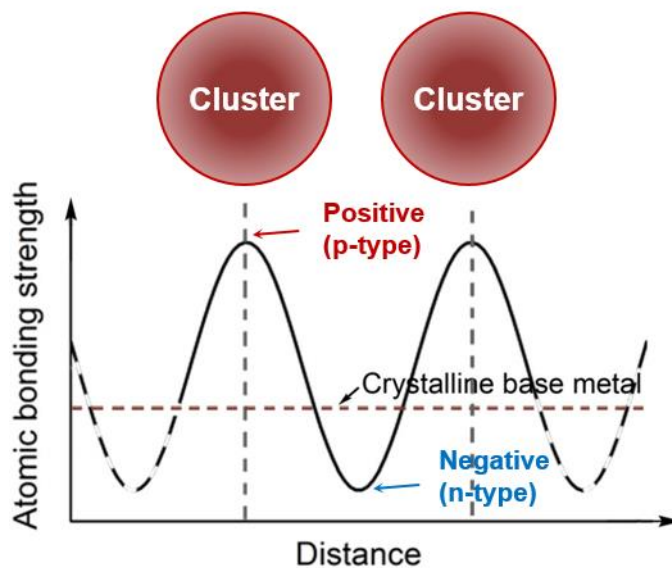


Fig. 3.1. Schematic illustration of the local atomic bonding strength between the clusters. (Reprinted from [56] with permission provided by AIP publishing and Copyright Clearance Center)

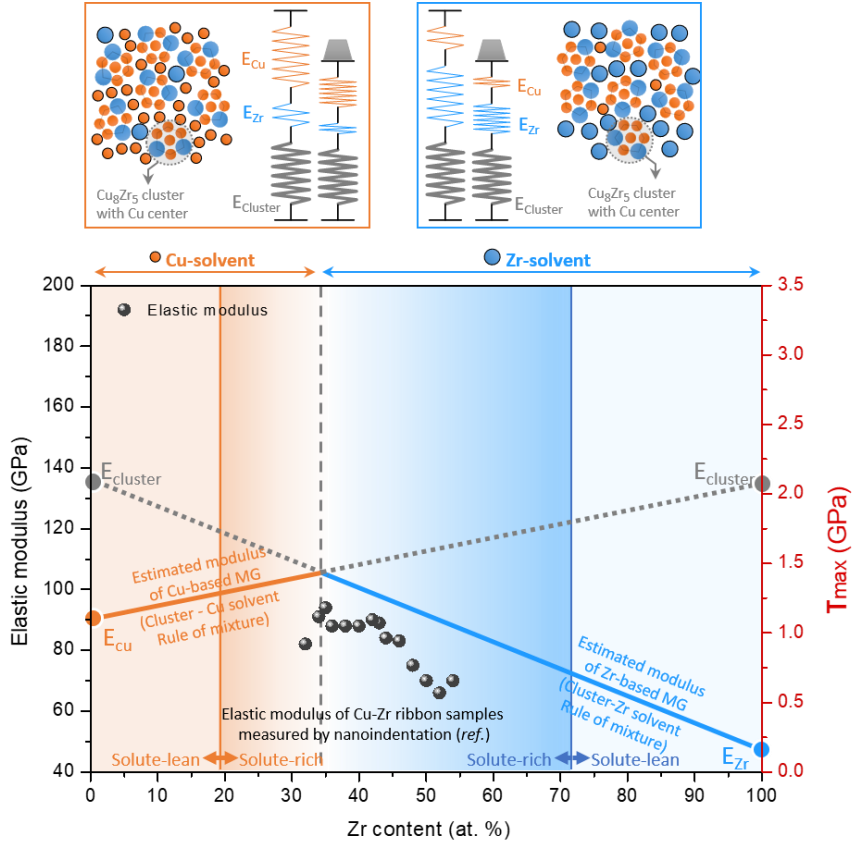


Fig. 3.2. Linear correlation of calculated modulus line and measured elastic modulus (Reprinted from [57] with permission provided by Elsevier and Copyright Clearance Center) according to composition change in Zr–Cu binary system

3.3. Glass formation in Zr–TM binary metallic glass

To verify glass formation and property changes in Zr–based metallic glass, we first fabricated the ribbon alloys of Zr–TM (= Cu, Ni, Co, Fe) binary systems. Cu, Ni, Co, and Fe are known as elements that can form a binary MG alloyed with Zr. [58–62] In this study, it was intended to investigate the characteristic temperature changes based on the base element content, Zr, in the binary Zr–based alloy systems. The phase analysis by XRD and heat flow curves measurement by DSC are shown in **Fig. 3.3**. MGs can be formed near eutectic composition with a low liquidus temperature of about 1400 K or less. **Fig. 3.4** shows composition range capable of glass formation by melt–spinning in each alloy system of Zr–Cu (**a**), Zr–Ni (**b**), Zr–Co (**c**), and Zr–Fe (**d**), and the characteristic temperature, T_g and T_x , of each composition. In particular, it has eutectic composition which form composite of beta–Zr phase and another intermetallic compound, but capable of glass formation with a Zr content between 69 and 79 at. % in all four systems.

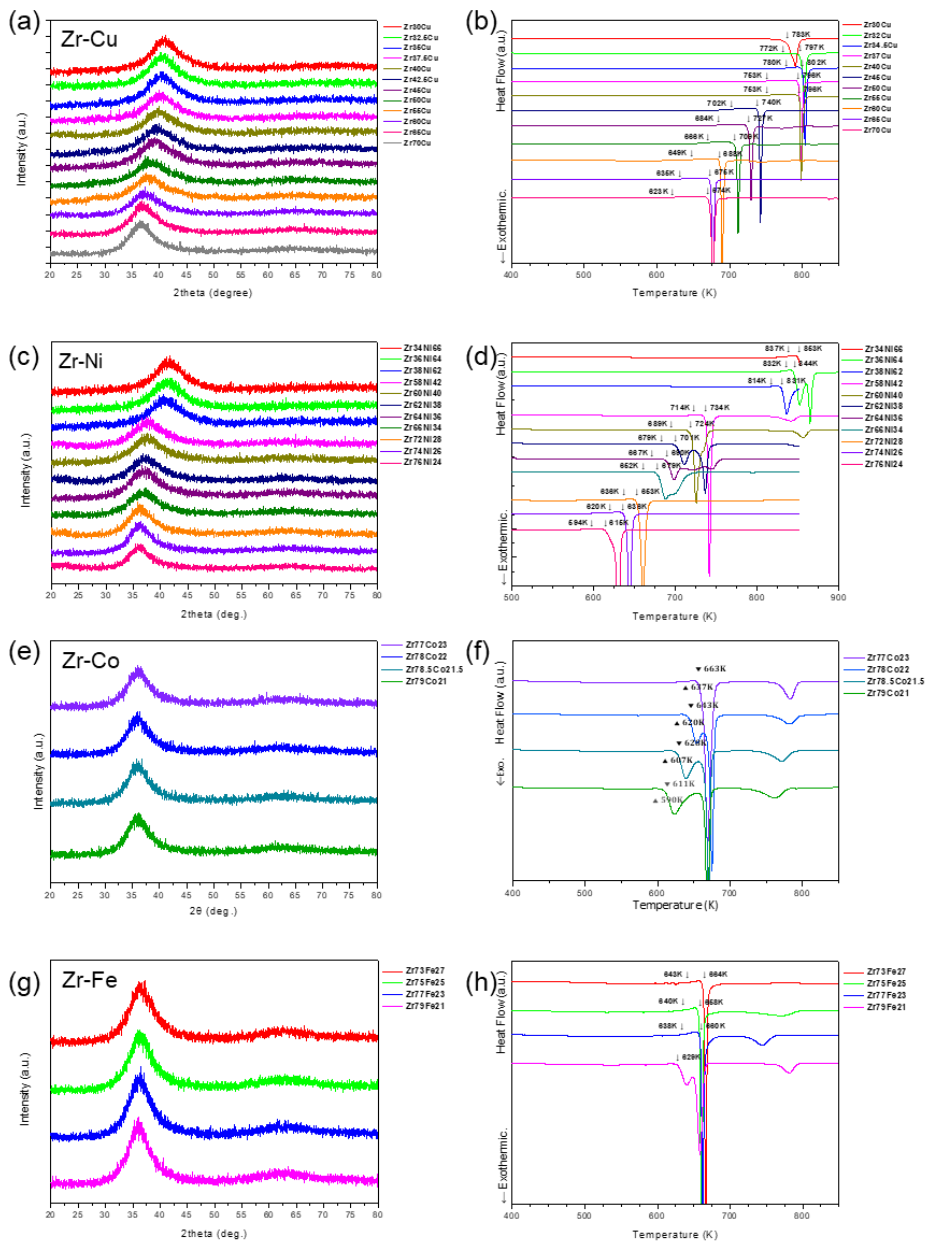


Fig. 3.3. Phase analysis by XRD and heat flow curves measurement by DSC of Zr–Cu, Zr–Ni, Zr–Co, and Zr–Fe binary MGs.

3.4. Thermal property changes in Zr–TM binary metallic glass

Fig. 3.4. shows T_g and T_x of the Zr–based MGs according to the Zr content. Previous studies have reported that solvent atoms form the weakest bonding of solvent–solvent bonding in amorphous structure to mainly determine elastic property, mechanical property, and thermal property. [63–65] Considering the atomic radius difference in the Zr–TM (= Cu, Ni, Co, Fe) binary system, when the Zr content is over than ~ 35 at. %, it can be considered that the element Zr plays a role as a solvent. [62] The solid blue line describes the T_g value and it is linearly fitted well, and accordingly, it is demonstrated that the variation of T_g changes according to the Zr content in all four Zr–TM (= Cu, Ni, Co, Fe) binary alloy systems. It can be expected that T_g value of MG may decrease when a composition changes with a direction of higher Zr content. Although it is practically difficult to be realized, the T_g of MG consisting of pure Zr element may have the lowest value to 517K in trend. Also, it was reported that the variation of T_g change depending on the Zr content fits well even in the multi–component Zr–based alloy system. [66] Therefore, we find that the T_g value is fundamentally determined by the Zr content composing weak bonding, but it is difficult to implement a lower T_g out of range of glass formation. (presented in **Fig. 3.5. (a)**) A boundary composition within glass formable range shows an extremely low T_g

ever. **Fig. 3.5. (b)** shows the heat flow curves measured by DSC instrument of the alloy composition with the highest Zr content in each of the four Zr–TM (= Cu, Ni, Co, Fe) binary alloy systems. Among these compositions, Zr₇₀Cu₃₀ alloy represents a relatively wide super-cooled liquid region, ΔT_x (= $T_x - T_g$), of about 50 K, and the other three alloys, Zr₇₆Ni₂₄, Zr₇₉Co₂₁, Zr₇₇Fe₂₃, exhibit thermal characteristics of a typical marginal MG where the crystallization behavior immediately follows the glass transition during heating.

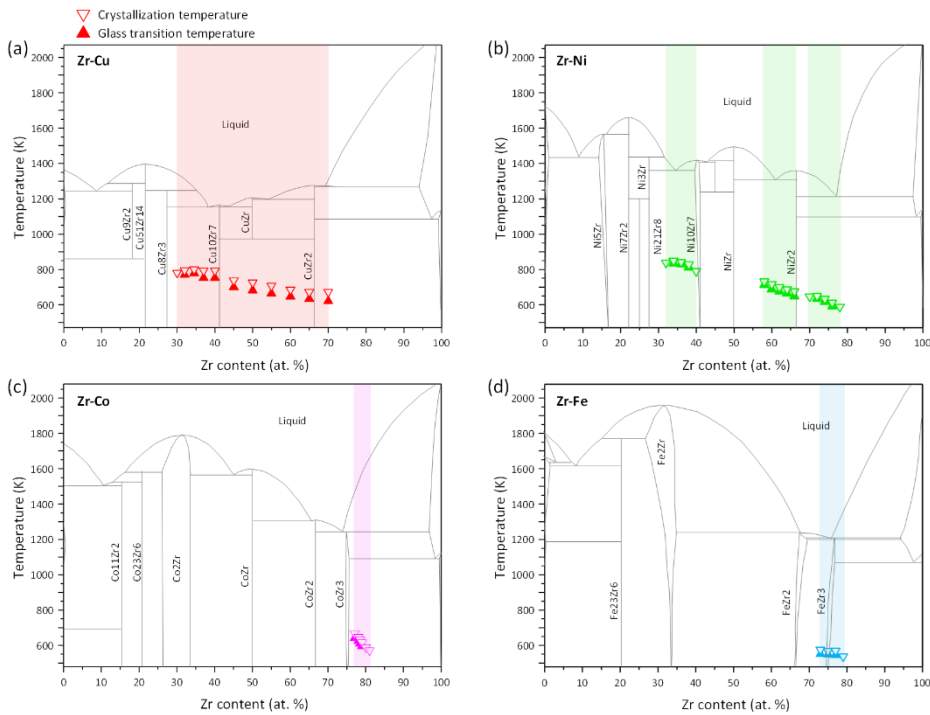


Fig. 3.4. Alloy compositions which can form metallic glass fabricated by melt-spinning in Zr–TM (= Cu, Ni, Co, and Fe) binary alloy systems and their characteristic temperature, T_g and T_x .

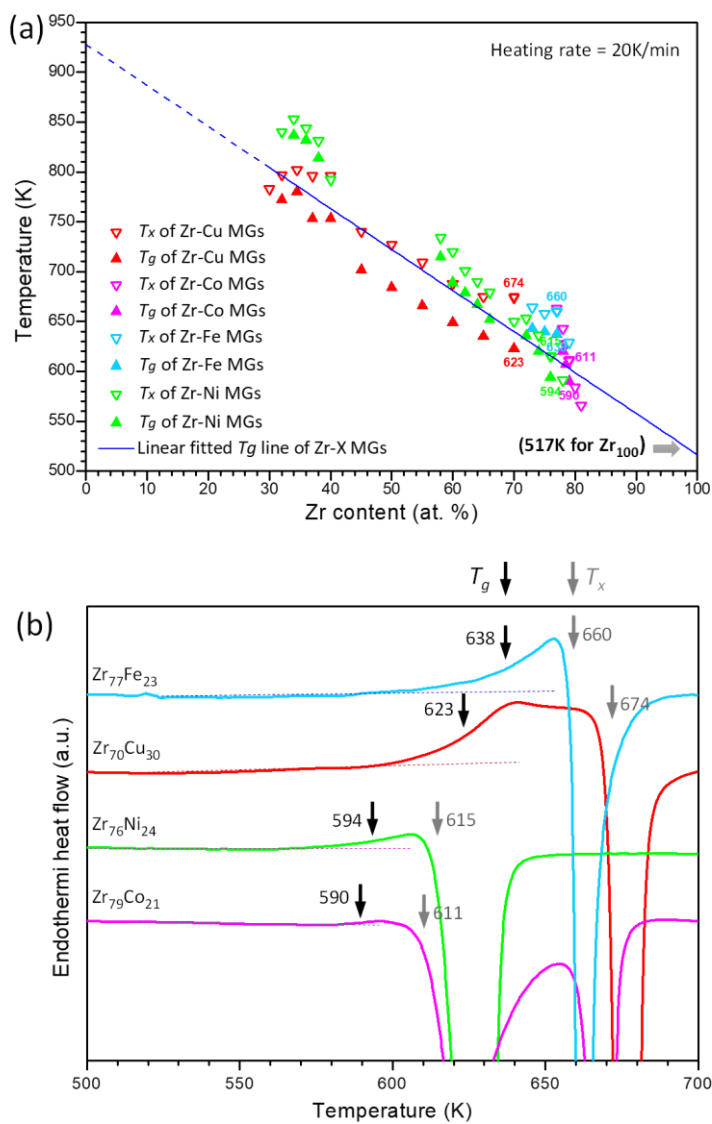


Fig. 3.5. (a) Linear correlation between T_g , T_x with Zr content in Zr-TM (= Cu, Ni, Co, and Fe) binary alloys. The blue line is the linear fitting of T_g in the Zr-TM (= Cu, Ni, Co, Fe) binary alloys. (b) Heat flow curves measured by DSC instruments of the composition with the highest Zr content in each alloy system.

Chapter 4.

Development of Zr-based metallic glasses applicable to thermoplastic process and facilities of engineering plastics

Among all the metallic materials, only metallic glasses (MGs) can be processed by thermoplastic forming (TPF) above the glass transition temperature (T_g) similar to conventional engineering plastics, which supplies advantages compared with the other alloys. [67–69] MGs also have the possibility to be used for various structural applications due to its outstanding mechanical properties such as high strength and large elastic limit. [70–75] By applying TPF, complicated shapes or detailed patterns, even micro- and nano-scale, can be easily achieved through only single processing step. [69] The direct casting method has various advantages that can be fabricated into simple shapes particularly for the bulk metallic glass (BMG). Otherwise, TPF is especially beneficial where it can be applied simply, but precisely to form complex-shaped small-sized products, such as MEMS (Micro Electro Mechanical Systems) parts, micro needles, and surface patterning. [76–79] The smaller the product size more freely allows to control the heating and cooling rates during the process, making it easier to avoid the crystallization,

the biggest challenge of TPF of MG. Therefore, it is considered that the commercialization of MGs with TPF has been mainly developed based on small-sized products, surface patterning, and fast heating process.

Commonly, process temperature of TPF in MGs is higher than around 400°C (673K), and the cost increases as the process temperature get higher. Further, the major problems limiting the commercialization of MGs is the initial cost for developing a commercial process and designing an exclusive facility. These problems can be solved in part by utilizing forming processes and facilities for conventional engineering plastics. Basically, the TPF processes of MGs such as compression molding and blow molding have been designed based on the conventional forming process of thermoplastic formable materials. [67–69, 80–82] If T_g of engineering plastics and MGs are similar to each other, it means that these two different materials fundamentally have a similar forming temperature. Therefore, the initial investment for commercializing MGs can be significantly reduced through utilizing the conventional forming process and facilities of engineering plastics. In this case, as entry barriers are lowered, the attempts to commercialize MGs can be promoted in the industry field.

It has been suggested that the evaluation of thermoplastic forming ability (TPFA) of MGs using the parameter, such as f ($= m * (T_x - T_g) / T_x$) [83], S ($= m * (T_x - T_g) / (T_1 - T_g)$) [84], and ΔT_F ($= T_1 -$

T_x) [85] determined by measuring liquidus temperature (T_l), T_g , crystallization temperature (T_x), and fragility parameter (m). However, in the previous studies, it has not been considered that TPFA can vary according to the heating rate. In the TPF process of MGs, various heating rates can be applied for each purposes. Particularly, both the values of T_g and T_x proportionally vary depending on the heating rate. Since T_g and T_x are closely related to TPFA as well as thermoforming window ($T_x - T_g$), which is a processing temperature range of MG, it is essential to specifically identify changes of the values depending on various heating rates. Recently, many studies regard to applying the fast heating rate to the TPF process of MG have been reported because it has advantages such as crystallization control, oxidation prevention, and also process time reduction. [86–90] Especially, it has been studied that ultrafast heating rate ($\sim 10^5$ K/s) can be applied through a capacitive discharge heating method [89, 90] or electronic pulses. [88] Thus, it is important to verify the thermoforming window and TPFA under various heating rate.

In this study, we developed Zr-based metallic glasses for TPF with T_g similar to that of conventional engineering plastic considering economic feasibility, mechanical properties, and TPFA. Further, the thermoforming window and TPFA were evaluated under various heating rates from 0.17 to 10^4 K/s. Finally, we constructed the continuous heating transformation (CHT) diagrams of the developed

MGs. It is expected to offers a fundamental understanding of thermoforming behavior of the developed MGs compared to the conventional engineering plastics.

4.1. Processing temperature for amorphous materials

Fig. 4.1. shows a thermoformable amorphous pyramid including both amorphous polymers (plastics) and metallic glasses based on T_g . Generally, T_g is a factor related to atomic bonding strength in amorphous materials. The higher the T_g , the higher the mechanical strength and elastic moduli, so it is superior as a structural material. However, the minimum process temperature for TPF increases as T_g gets higher. TPF at high temperature not only consumes significant large energy to maintain the process condition, but also requires high heat resistance of equipment. At the same time, it promotes oxidation of material surface. Thus, the cost of TPF increases rapidly with temperature. [91] Standard and engineering plastics such as PC, PVC, or acrylic are utilized as general industrial structural materials. [26, 27] Advanced engineering plastics, for example imidized plastics, PI, PBI, with a high forming temperature are mainly utilized for specific purpose, where high physical properties are required such as thrust

bearing and washers in automobiles. [92] In Fig. 4.1., plastics are arranged according to its T_g , and MGs are classified based on the alloy system corresponding to plastics with similar T_g . Mechanical properties of Ce-, Ca-, and Mg-based MGs are severely brittle, so they are difficult to be utilized as structural materials. [93] In addition, the fact that the base element price of Au-, Pt-, and Pd-based MGs is too expensive is an obstacle for them to be widely used as structural materials. Even if these MGs have an advantage in TPF and TPFA due to relatively low T_g , but, considering economic feasibility and mechanical properties, they are difficult to be practically commercialized. Zr-based MGs have the lowest T_g among thermoformable alloys which can be commercialized as structural materials. The Zr-based MGs with outstanding glass forming ability (GFA) has a T_g of above 350°C. But, Zr-based MGs with low T_g contain lots of amount of Be, which is a toxic element. For commercialization of Zr-based MGs, Alloy design without containing Be is necessary. It is expected that Zr-based MGs can be applied to TPF by utilizing the existing forming processes and facilities for conventional plastics with similar T_g .

Thermoformable Amorphous Pyramid

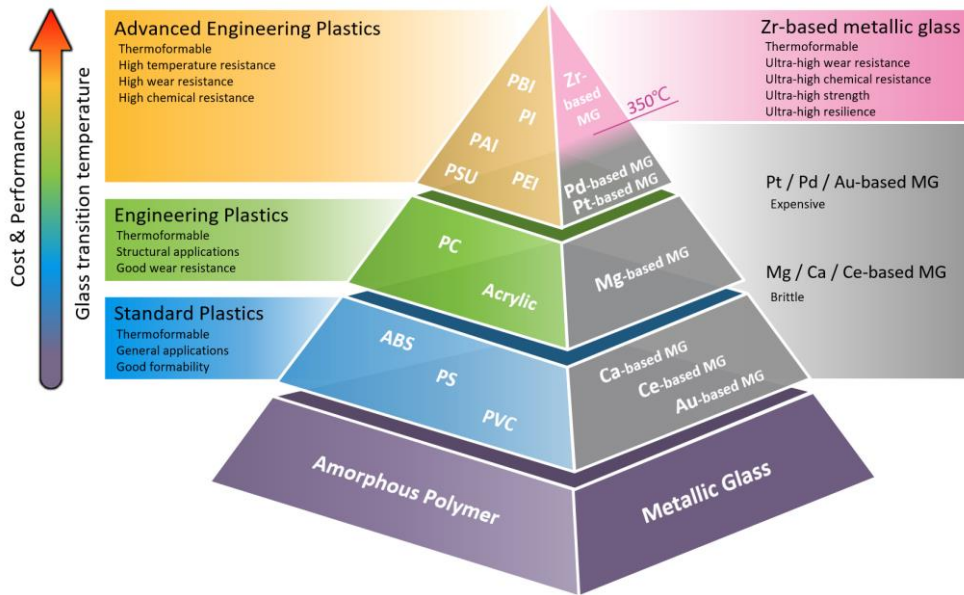


Fig. 4.1. Schematic diagram of thermoformable amorphous pyramid according to the glass transition temperature, which shows comparison of amorphous polymer plastics and amorphous alloys (metallic glasses). The higher the glass transition temperature, the better the performance, but the higher process cost.

Fig. 4.2. shows the strength and Young's modulus of representative amorphous plastics and MGs depending on T_g . Because the difference between compressive and tensile strength was considered to be negligible in comparison with the difference in the strength between the different materials, compressive strength for MG and tensile strength for plastics were both indicated. In **Table 4.1** and **Table 4.2**, details of both the composition and properties for each plastic [94–

98] and MGs [99, 100] are given. MGs exhibit about 10 times higher strength and Young's modulus than plastics which have similar T_g . Zr-based MGs can be utilized as structural materials which can replace PI and PBI, and also can be the potential candidates to be applied for structural parts which require both high strength and wear resistance that conventional engineering plastics could not be utilized, such as micro gears.

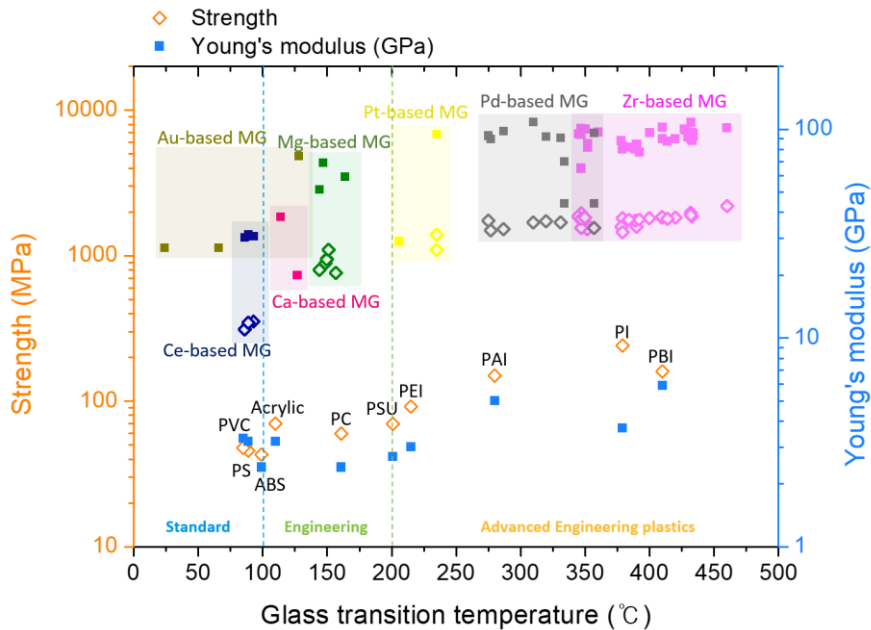


Fig. 4.2. Strength and Young's modulus values of conventional amorphous polymer plastics and MGs, arranged according to the T_g . The mechanical properties of plastics and MGs which have similar values of T_g are compared.

Short name	Full name	T _g (°C)	Tensile strength (MPa)	Young's modulus (GPa)
PBI	Polybenzimidazole	410	160	5.9
PI	Polyimides	379	241	3.7
PAI	Polyamide–imide	280	150	5
PEI	Polyetherimide	215	92	3
PSU	Polysulfone	201	70	2.7
PC	Polycarbonate	161	60	2.4
Acrylic	Acrylic polymers	110	70	3.2
ABS	Acrylonitrile butadiene styrene	104	43	2.4
PS	Polystyrene	89	46	3.2
PVC	Polyvinyl Chloride	85	48	3.3

Table 4.1. T_g, tensile strength and Young's modulus of representative amorphous plastics [94–98]

Alloy composition (at. %)	T _g (°C)	Compressive strength (MPa)	Young's modulus (GPa)
Zr ₄₈ Nb ₈ Ni ₁₂ Cu ₁₄ Be ₁₈	347	1950	93.9
Zr ₅₅ Al ₁₉ Co ₁₉ Cu ₇	460	2200	101.7
Zr _{57.5} Nb ₅ Cu _{15.4} Ni ₁₂ Al ₁₀	390	1580	84.7
Zr ₅₅ Ti ₅ Cu ₂₀ Ni ₁₀ Al ₁₀	352	1630	85
Zr _{41.2} Ti _{13.8} Cu _{12.5} Ni ₁₀ Be _{22.5}	345	1860	95
Zr ₆₂ Cu _{15.4} Ni _{12.6} Al ₁₀	379	1812	80

$Zr_{59}Ta_5Cu_{18}Ni_8Al_{10}$	400	1817	96
$Zr_{41.2}Ti_{13.8}Cu_{12.5}Ni_{10}Be_{22.5}$	347	1755	97
$(Zr_{0.5}Cu_{0.5})_{95}Al_5$	420	1824	90
$Zr_{50}Cu_{40}Al_{10}$	433	1860	88
$Zr_{55}Cu_{30}Al_{10}Ni_5$	410	1830	90
$Zr_{60}Cu_{20}Al_{10}Ni_{10}$	389	1750	80
$Zr_{65}Cu_{17.5}Al_{7.5}Ni_{10}$	352	1528	82
$Zr_{48}Cu_{36}Al_8Ag_8$	410	1850	102
$Zr_{42}Cu_{42}Al_8Ag_8$	432	1986	108
$Zr_{62.5}Cu_{22.5}Al_{10}Fe_5$	378	1584	88
$Zr_{57}Ti_5Al_{10}Cu_{20}Ni_8$	347	1560	65
$Zr_{46}Cu_{37.64}Ag_{8.36}Al_8$	430	—	91.5
$Zr_{46}Cu_{34.64}Ag_{8.36}Al_8Be_3$	434	—	92.5
$Zr_{46}Cu_{32.64}Ag_{8.36}Al_8Be_5$	434	—	95.1
$Zr_{46}Cu_{31.64}Ag_{8.36}Al_8Be_6$	433	—	96
$Zr_{46}Cu_{30.14}Ag_{8.36}Al_8Be_{7.5}$	432	—	96.3
$Zr_{46}Cu_{27.64}Ag_{8.36}Al_8Be_{10}$	430	—	97.1
$Zr_{46}Cu_{25.14}Ag_{8.36}Al_8Be_{12.5}$	428	—	98.7
$Zr_{46}Cu_{22.64}Ag_{8.36}Al_8Be_{15}$	427	—	100
$Zr_{41}Ti_{14}Cu_{12.5}Ni_{10}Be_{22.5}$	347	1800	101
$Zr_{46.75}Ti_{8.25}Cu_{7.5}Ni_{10}Be_{27.5}$	350	1830	100
$Zr_{65}Al_{10}Ni_{10}Cu_{15}$	379	1450	83
$Zr_{52.25}Cu_{28.5}Ni_{4.75}Al_{9.5}Ta_5$	432	1909	90

$Zr_{61}Cu_{17.3}Ni_{12.8}Al_{7.9}Sn_1$	392	1770	77.4
$Zr_{57}Ti_5Cu_{20}Ni_8Al_{10}$	384	1770	82
$Zr_{57}Nb_5Cu_{15.4}Ni_{12.6}Al_{10}$	414	1800	87.3
$Zr_{50}Cu_{25}Be_{25}$	360	–	96.8
$Pd_{40}Cu_{30}Ni_{10}P_{20}$	320	1720	92
$Pd_{60}Cu_{20}P_{20}$	331	1700	91
$Pd_{77.5}Cu_6Si_{16.5}$	277	1500	89.7
$Pd_{40}Cu_{40}P_{20}$	275	1750	93
$Pd_{40}Ni_{10}Cu_{30}P_{20}$	287	1520	98
$Pd_{77.5}Si_{16.5}Cu_6$	357	1550	96
$Pd_{40}Ni_{40}P_{20}$	310	1700	108
$Pd_{64}Fe_{16}P_{20}$	357	–	44
$Pd_{80}Si_{20}$	334	–	70
$Pd_{80}P_{20}$	334	–	44
$Pt_{57.5}Cu_{14.7}Ni_{5.3}P_{22.5}$	235	1100	–
$Pt_{74.7}Cu_{1.5}Ag_{0.3}P_{18}B_4Si_{1.5}$	206	–	29
$Pt_{57.5}Cu_{14.7}Ni_{5.3}P_{22.5}$	235	1400	94.8
$Mg_{65}Cu_{15}Ag_5Pd_5Gd_{10}$	157	765	–
$Mg_{61}Cu_{28}Gd_{11}$	149	891	–
$Mg_{66}Cu_{19.55}Ni_{3.45}Gd_{11}$	150	955	–
$Mg_{65}Cu_{18}Ni_6Gd_{11}$	150	938	–
$Mg_{63}Cu_{16.8}Ag_{11.2}Er_9$	151.1	1098	–
$Mg_{65}Cu_{25}Tb_{10}$	144	800	51.3

$\text{Mg}_{65}\text{Y}_{10}\text{Cu}_{15}\text{Ag}_5\text{Pd}_5$	164	–	59
$\text{Mg}_{65}\text{Cu}_{20}\text{Y}_{15}$	147	–	69
$\text{Ca}_{65}\text{Ag}_{35}$	127	–	20
$\text{Ca}_{57}\text{Mg}_{19}\text{Cu}_{24}$	114	–	38
$\text{Ce}_{70}\text{Al}_{10}\text{Ni}_{10}\text{Cu}_{10}$	86	313	30.3
$(\text{Ce}_{20}\text{La}_{80})\text{Al}_{10}\text{Cu}_{20}\text{Co}_2$	93	354	30.69
$(\text{Ce}_{50}\text{La}_{50})\text{Al}_{10}\text{Cu}_{20}\text{Co}_2$	89	348	31.27
$\text{Au}_{76.9}\text{Si}_{9.45}\text{Ge}_{13.66}$	24	–	27
$\text{Au}_{49}\text{Ag}_{5.5}\text{Pd}_{2.3}\text{Cu}_{26.9}\text{Si}_{16.3}$	128	–	74.4
$\text{Au}_{70}\text{Cu}_{5.5}\text{Ag}_{7.5}\text{Si}_{17}$	66	–	27

Table 4.2. T_g , compressive strength and Young's modulus of MGs [99–100]

Fig. 4.3 (a) shows schematics of continuous heating transformation (CHT) diagrams and isothermal time–temperature–transformation (TTT) diagrams for crystallization of MG. [101, 102] Further, the cooling path of casting, subsequent heating and annealing path of TPF are shown. **Fig. 4.3 (b)** shows a schematic procedure of a typical compression molding performed after fabrication of MG. For MG fabrication, molten alloy should be solidified quickly than the critical cooling rate to avoid formation of crystalline phase. MG can be heated between super–cooled liquid region, T_g and T_x , with reduced viscosity. In this temperature range, viscous flow can be employed

for TPF. The viscosity of the super-cooled liquid decreases up to the temperature close to T_x , so it is theoretically desirable to apply TPF near T_x within a time when crystalline phase cannot be formed. The thermoforming window, which is the temperature and time range where TPF is possible, can be regarded as within the CHT T_g to T_x curves. The previous studies on TPF have been mainly implemented on the conventional thermal forming window that can be conducted by a slow heating rate of 10 K/s or less. However, because studies on fast heating of MGs for micro forming and capacitive discharge have recently been investigated, this study will discuss the potential method using a thermoforming window that can be realized at an ultra-fast heating rate of 10^2 K/s or more.

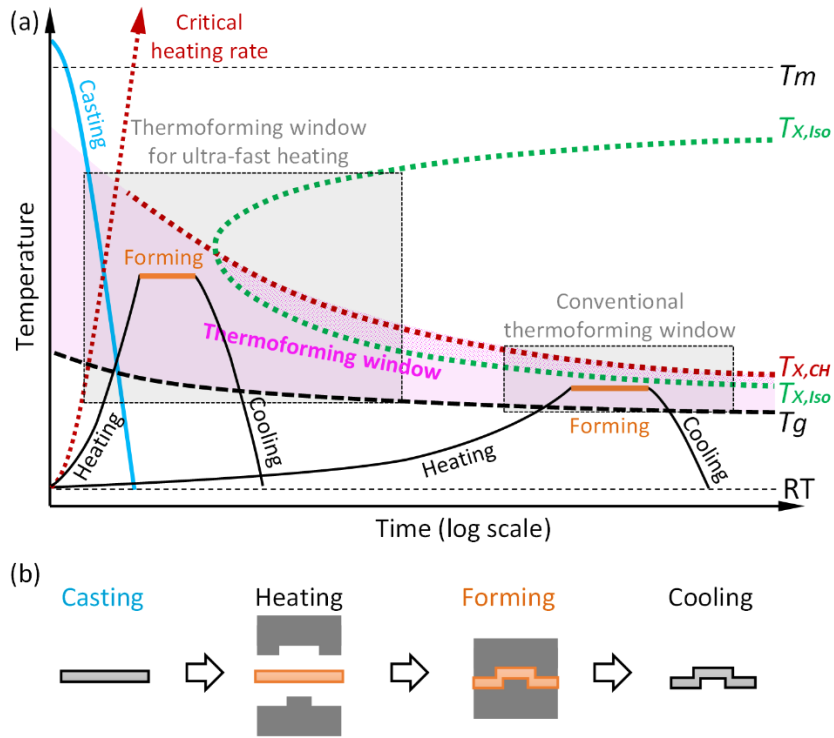


Fig. 4.3. Schematic diagram for TPF process of metallic glass. (a) Illustration of thermoforming window of MG. Isochronal CHT curve, isothermal TTT curve and T_g curves are plotted. TPF is performed in the temperature range within T_g to T_x . Schematics of casting, TPF by conventional heating and ultra-fast heating are illustrated. (b) The schematic illustration of TPF process of MG after casting.

4.2. Compositional dependence of thermal property

To verify the lowest T_g that can be realized in Be-free Zr-based alloy systems and develop novel MGs with a sufficiently broad thermoforming window, we progress in sequence alloy design from binary to multi-component alloys. Transition metal such Cu, Ni, Co, and Fe are regarded as component that can be alloyed with Zr element to form a binary MG, except for Be, Pd, and Pt in consideration of toxicity and economic cost. [58–62] In this research, we first plan to investigate the limit of the lowest T_g value based on the fabrication of MGs in the binary Zr-TM (= Cu, Ni, Co, Fe) binary alloy systems. **Fig. 3.4.** shows a composition capability for glass formation fabricated by melt-spinning in binary alloy systems of Zr-Cu **(a)**, Zr-Ni **(b)**, Zr-Co **(c)**, and Zr-Fe **(d)**. And the characteristic temperatures of T_g and T_x are plotted in each composition. Particularly, these binary systems have eutectic composition of beta-Zr phase and another intermetallic compound possible to fabricate glassy ribbon alloy with a Zr content between 69 and 79 at. %. **Fig. 3.5. (a)** shows value of T_g and T_x in the Zr-TM (= Cu, Ni, Co, Fe) binary MGs according to the Zr content. Previous studies have been reported that solvent elements form the weakest bonding consisting of solvent-solvent in amorphous structure to directly affect modulus, strength, and T_g . [63–65] Considering the atomic radius difference in the Zr-Cu binary system, when the Zr content is

over than 35 at. %, it can be considered that the Zr element serves as a solvent among constituent. [62] The solid blue line indicates that the value of T_g is linearly fitted well, and it is identified that the tendency of change of T_g to be determined depending on the Zr content is verified to all four alloy systems accordingly. It can be argued that MG may have a lower value of T_g in a composition of higher Zr content. Although it is practically impossible to be formed, the value of T_g of the pure Zr MG may have the lowest T_g around 517K. Recently, it was studied that the variation of T_g change depending on the Zr content fits in well even in the multi-component Zr-based glass forming system. [66] We found that value of T_g is fundamentally determined by the Zr element composing weak bonding and it is very difficult to develop MG with a lower T_g than the MGs presented in **Fig. 3.5. (a)**. However, one of the binary MGs with an extremely high Zr content developed in this study is suitable for TPF. The heat flow curves of the alloy composition with the highest Zr content in each of the four alloy systems obtained by DSC measurement are plotted in **Fig. 3.5. (b)**. Among them, $Zr_{70}Cu_{30}$ MG exhibits a relatively wide super-cooled liquid region, ΔT_x of about 50 K, and the other three compositions show thermal property of a typical marginal MG where crystallization immediately occurs after glass transition during heating.

4.3. Thermal property optimization in Zr-based multicomponent system

We intended to design multi-component Zr-based MG based on Zr-TM (= Cu, Ni, Co, Fe) binary MG suitable for TPF. **Fig. 4.4.** exhibits the T_g and ΔT_x values of the binary MGs developed in this work depending on the content of Zr. ΔT_x has no significant correlation with the Zr content, and it shows a relatively large super-cooled liquid region in the Zr-Cu system compared to other alloy systems. In particular, the $Zr_{70}Cu_{30}$ with the highest Zr content has the widest ΔT_x value among Zr-TM (= Cu, Ni, Co, Fe) binary MGs, and this composition can be potential candidate as having a combination of low T_g and wide ΔT_x values.

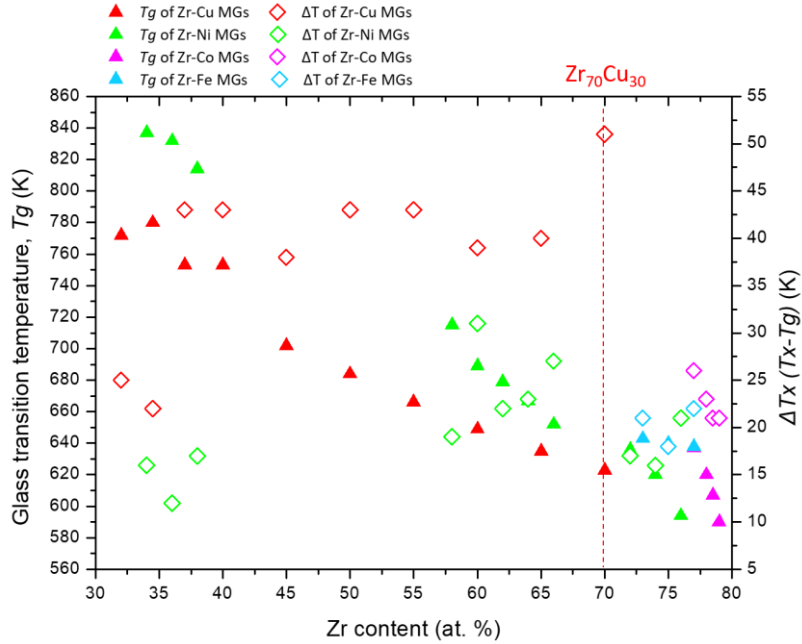


Fig. 4.4. T_g and ΔT_x of Zr–TM (= Cu, Ni, Co, Fe) binary alloys. $Zr_{70}Cu_{30}$ alloy shows potentially thermal property of thermoformable binary MG because of its low T_g and wide ΔT_x .

Fig. 4.5. represents the experimental measurement to investigate the change in the values of T_g and ΔT_x by alloying with Ni (**a–e**) and Co (**f–j**) based on $Zr_{70}Cu_{30}$. **Fig. 4.7 (a, f)** exhibits the developed alloy compositions on the liquidus projection of ternary systems, Zr–Cu–Ni and Zr–Cu–Co, respectively. The liquidus projections of the two alloy systems are highly similar, and accordingly, the effect of alloying with Ni and Co is expected to be similar to each other. **Fig. 4.5. (b, c, g, h)** shows the XRD measurement and DSC heat flow curves of the ternary alloys designed to further increase the Zr

content from the eutectic composition where the beta-Zr crystalline phase as one of the eutectic component in each alloy system. In both cases, beta-Zr crystalline phase formed in the as-spun ribbon alloys when the Zr element content increased by about 4 at. % or more from the eutectic valley. This result suggests that the Zr content capability for glass formation is limited along the eutectic valley because of the beta-Zr phase. **Fig. 4.5. (d, e, i, j)** represents the XRD patterns and DSC heat flow curves of an alloy developed by designing a content of Ni and Co to increase along the eutectic liquidus line in each alloy system. A broad halo peak meaning the formation of a glassy structure is identified in the XRD patterns for all alloys. As the content of Ni content and Co content increases, the Zr content increases along the eutectic liquidus line, and therefore T_g value tends to decrease accordingly. ΔT_x value is slightly increased when 4.8 at. % for Ni content and 4.2 at. % for Co content are substituted, but overall tends to decrease significantly when more Ni and Co are added. In conclusion, it is confirmed that the substitution of about 4 at. % of Ni or Co affect to lower the T_g value of Zr-Cu binary MG and increasing the ΔT_x .

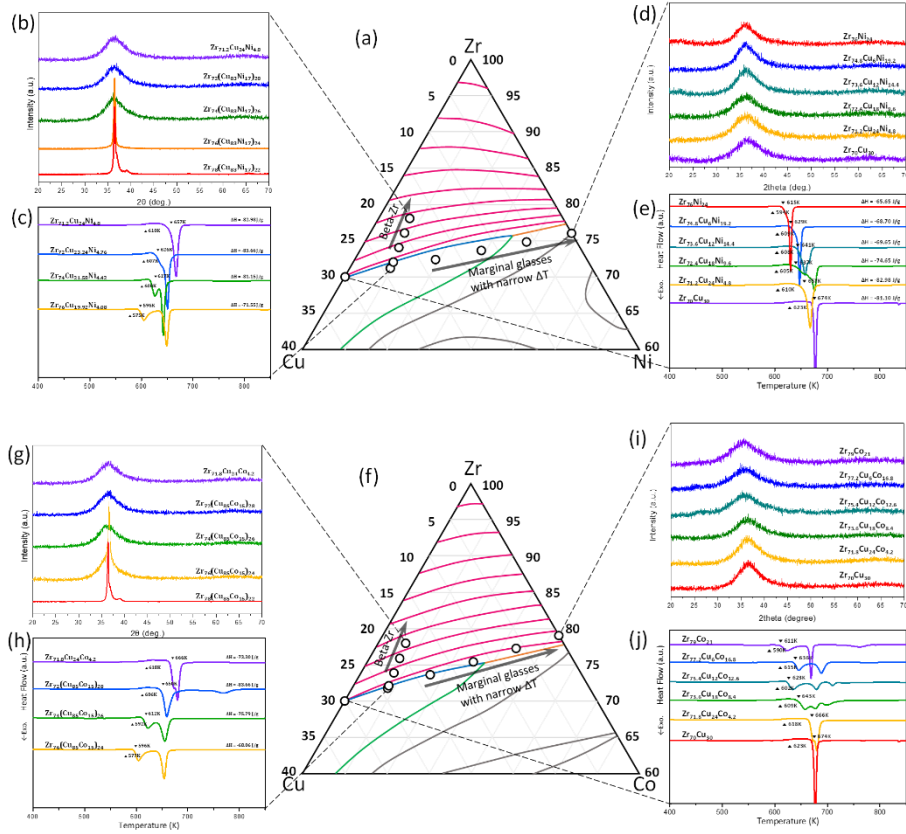


Fig. 4.5. Measurement of variations in T_g and ΔT_x of ternary alloys in ZrCuNi and ZrCuCo systems. **(a)** The compositions of ZrCuNi alloys fabricated by melt-spinning are plotted on the Zr–Cu–Ni liquidus projection. **(b, c)** XRD patterns and heat flow curves of ZrCuNi alloys represented according to increase of the Zr content from the $Zr_{71.2}Cu_{24}Ni_{4.8}$ composition. **(d, e)** XRD patterns and heat flow curves of ZrCuNi alloys represented between $Zr_{70}Cu_{30}$ and $Zr_{76}Ni_{24}$. **(f)** The compositions of ZrCuCo alloys fabricated by melt-spinning are expressed on the Zr–Cu–Co liquidus projection. **(g, h)** XRD patterns and heat flow curves of ZrCuCo alloys represented according to increase of the Zr content from the $Zr_{71.8}Cu_{24}Co_{4.2}$

composition. (i, j) XRD patterns and heat flow curves of ZrCuCo alloys represented between $Zr_{70}Cu_{30}$ and $Zr_{79}Co_{21}$.

MGs of multicomponent were designed by alloying with Ni, Co, Fe, and Al based on $Zr_{70}Cu_{30}$ MG, and the T_g and ΔT_x values of each alloy are shown with regard to the Zr content in **Fig. 4.6. (a)**. It can be represented that the linear correlation between T_g and Zr content of developed Zr-based MGs is well fitted even when multicomponent alloys are added. In particular, in this study, the Zr content was fixed at 70 at. % and the ΔT_x was improved to 70 K or more through alloying of other elements. **Fig. 4.6. (b)** shows the value of T_g and ΔT_x of each composition according to the alloy system. Finally, a composition of $Zr_{70}Cu_{16}Ni_4Co_4Al_6$ with a low T_g of 625 K and a wide ΔT_x of 70 K was developed. As shown in **Fig. 4.5.**, this composition is alloyed with 4 at. % of Ni and Co, respectively. When the Zr content further increases from 70 at. %, ΔT_x decreases drastically. when the alloying element Fe is substituted, T_g increases, but ΔT_x decreases. However, the Addition of Al slightly increases T_g but greatly increases ΔT_x by about 6 at. %. Therefore, it is possible to design MGs significantly improved ΔT_x while maintaining the low T_g through the following alloy design, Zr content is fixed based on $Zr_{70}Cu_{30}$ and alloying elements of Ni and Co are added at 4 at. % and Al added at 6 at. %. In the next chapter, the TPFA and thermoforming window of the developed alloy, $Zr_{70}Cu_{16}Ni_4Co_4Al_6$, will be evaluated

according to the heating rate.

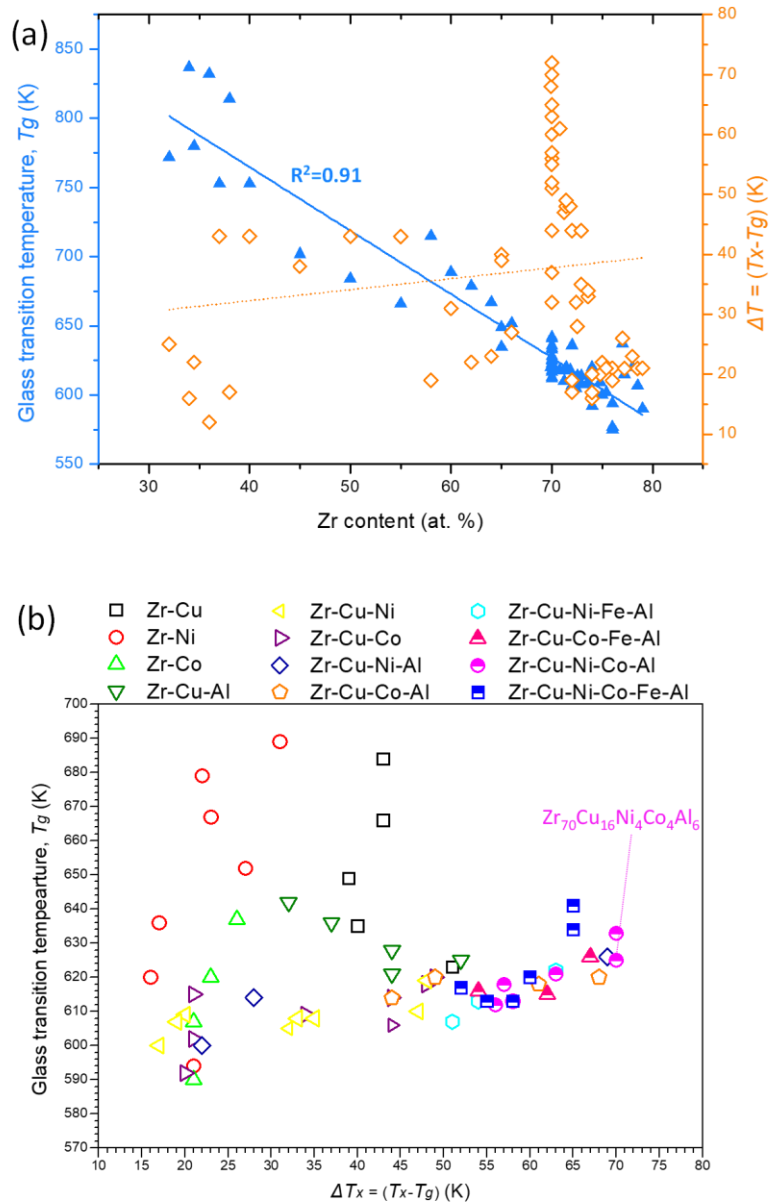


Fig. 4.6. The value of T_g and ΔT_x of Zr-based MGs designed in binary to senior alloy systems. (a) T_g exhibits a linear correlation inversely proportional to Zr content, whereas ΔT_x changes greatly

depending on the combination of additional alloying elements. (b) $Zr_{70}Cu_{16}Ni_4Co_4Al_6$ is selected as the representative composition in this study for thermoforming because of the low T_g and wide ΔT_x of 70 K.

4.4. Formability evaluation

The viscous flow of MG in super-cooled liquid region at a temperature between T_g and T_x is classified into the Newtonian viscous flow (NVF) and non-NVF. In theory, NVF in constant strain rate condition is preferred for TPF because of its the advantages of flow stability, but most of the practical processes are performed through mixed conditions both of NVF and non-NVF depending on the needs of the process considering the forming temperature, heating rate, strain rate, and the complexity of geometry. [85, 103–105] Because the TPF conditions cannot be specified at the stage of alloy development, it is not easy to evaluate the TPFA of MGs considering all the variables. Therefore, as shown in **Fig. 4.7.**, MGs in various alloy systems and those alloys developed in this study were compared through two different parameters, ΔT_F ($= T_1 - T_x$) [85] (measured with the heating rate of 0.3 K/s), and a parameter to evaluate ideal TPFA in NVF conditions, expressed with $(T_x^2 / m T)$

$/(T_1 - T_x)^2$ which have an inverse correlation with ΔT_F . **Table 4.3.** represents the parameters for each alloy composition. [84, 100, 106–122] Pd-based MGs are considered to have the highest TPFA due to their high T_x and low T_1 , and the RE-based MGs with high T_1 and low T_x have lower TPFA rather than the other alloys. For the value of fragility, m , of MGs developed in this study, the values of similar composition in previous papers were used. [114, 123–124] $Zr_{76}Ni_{24}$ and $Zr_{70}Cu_{30}$ binary MGs in this study have a low level of TPFA similar level to Fe and Al-based MGs, and $Zr_{70}Cu_{16}Ni_4Co_4Al_6$ MG has expectation to have comparable TPFA to conventional Be-free Zr-based MGs.

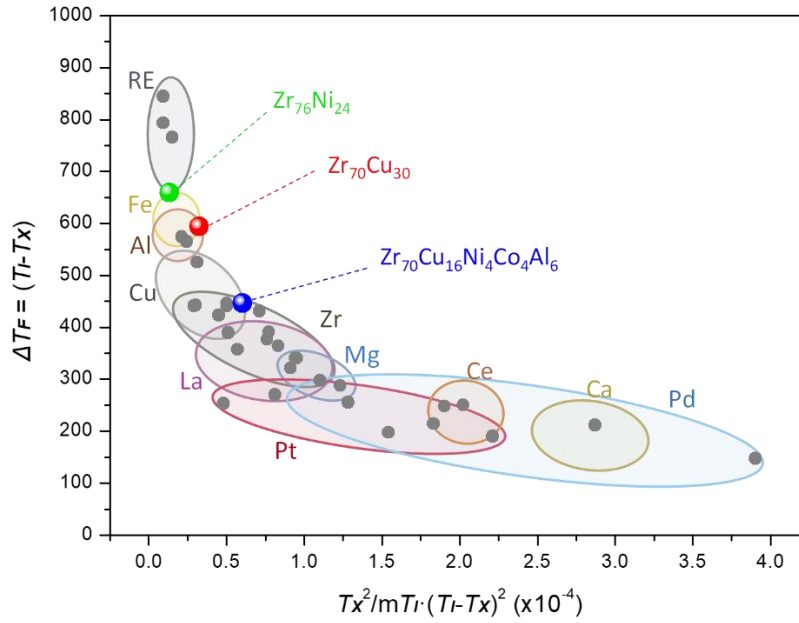


Fig. 4.7. Comparison of the TPFA between the MGs developed in this study and the previously reported BMGs through two different parameters, $\Delta T_F (= T_l - T_x)$, a TPFA parameter which is possible to be evaluated simply by measuring T_l and T_x , and $(T_x^2 / m T_l) / (T_l - T_x)^2$, a TPFA parameter considered as a factor in ideal condition. The fragility value, m , for some alloys is estimated.

Metallic glasses	T_x (K)	T_1 (K)	m	$T_x^2/mT_1*(T_1-T_x)^2$ ($\times 10^{-4}$)	ΔT_F	Ref.
Al ₈₄ Ni ₁₀ La ₆	552	1118	35	249.46	566	[115]
Au ₄₉ Ag _{5.5} Pd _{2.3} Cu _{26.9} Si _{16.3}	457	655	52.8	1.54	198	[84]
Ca ₆₅ Mg ₁₅ Zn ₂₀	412	624	21.1	2.87	212	[121]
Ce ₇₀ Al ₁₀ Ni ₁₀ Cu ₁₀	426	677	21	2.02	251	[113]
Cu ₄₆ Zr ₄₂ Al ₇ Y ₅	772	1113	49	0.94	341	[108]
Cu ₄₇ Ti ₃₄ Zr ₁₁ Ni ₈	717	1160	59	0.3	443	[109]
Cu ₅₄ Ni ₆ Ti ₁₈ Zr ₂₂	769	1295	53.4	0.31	526	[122]
Fe ₇₂ Hf ₈ Nb ₂ B ₁₈	932	1448	45	0.21	575	[111]
Ho ₃₉ Al ₂₅ Co ₂₀ Y ₁₆	706	1551	49	0.09	845	[120]
La ₅₅ Al ₂₅ Cu ₁₀ Ni ₁₀	547	835	35	1.23	288	[109]
La ₅₅ Al ₂₅ Ni ₂₀	551	941	42	0.51	390	[117]
La ₅₅ Al ₂₅ Ni ₅ Cu ₁₅	520	878	42	0.57	358	[117]
Mg ₆₅ Cu ₂₅ Gd ₁₀	484	740	37.6	1.28	256	[118]
Mg ₆₅ Cu ₂₅ Y ₁₀	468	739	50	0.81	271	[119]
Nd ₆₀ Fe ₂₀ Co ₁₀ Al ₁₀	645	1411	33	0.15	766	[120]
Pd ₄₀ Ni ₁₀ Cu ₃₀ P ₂₀	657	848	63	2.21	191	[109]
Pd ₄₀ Ni ₄₀ P ₂₀	651	973	46	0.91	322	[110]
Pd ₄₃ Ni ₁₀ Cu ₂₇ P ₂₀	679	827	65.2	3.9	148	[84]
Pd _{77.5} Si _{16.5} Cu ₆	686	1128	73	0.29	442	[100]
Pr ₆₀ Al ₁₀ Ni ₁₀ Cu ₂₀	469	1263	31	0.09	794	[120]
Pt _{57.5} Cu _{14.7} Ni _{5.3} P _{22.5}	598	813	51.9	1.83	215	[84]
Pt ₆₀ Ni ₁₅ P ₂₅	550	875	67.2	0.48	254	[113]
Zr _{41.25} Ti _{13.75} Cu _{12.5} Ni ₁₀ Be _{22.5}	698	996	50	1.1	298	[106]
Zr ₄₄ Ti ₁₁ Cu ₁₀ Ni ₁₀ Be ₂₅	744	993	47.2	1.9	249	[84]
Zr ₄₆ (Cu _{4.5/5.5} Ag _{1/5.5}) ₄₆ Al ₈	782	1123	49	0.95	341	[116]
Zr _{46.75} Ti _{8.25} Ni ₁₀ Cu _{7.5} Be _{27.5}	738	1185	45.6	0.5	447	[112]
Zr ₄₆ Cu ₄₆ Al ₈	771	1163	43	0.77	392	[109]
Zr ₅₅ Al ₁₀ Cu ₃₀ Ni ₅	768	1210	50	0.5	442	[107]
Zr ₅₇ Nb ₅ Cu _{15.4} Ni _{12.6} Al ₁₀	743	1120	45.9	0.76	377	[84]
Zr _{58.5} Nb _{2.8} Cu _{15.6} Ni _{12.8} Al _{10.3}	753	1118	45.9	0.83	365	[84]
Zr ₆₅ Al ₁₀ Ni ₁₀ Cu ₁₅	757	1181	59.4	0.45	424	[84]
Zr ₆₅ Al _{7.5} Ni ₁₀ Cu _{17.5}	736	1168	35	0.71	432	[114]
Zr ₇₆ Ni ₂₄ (this work)	623	1283	53 ^{[123] 1)}	0.13	660	–
Zr ₇₀ Cu ₃₀ (this work)	698.14	1292	33 ^[124]	0.32	593.86	–
Zr ₇₀ Cu ₁₆ Ni ₄ Co ₄ Al ₆ (this work)	693.88	1141	35 ^{[114] 2)}	0.60	447.12	–

1) m value of Zr₇₇Ni₂₃

2) m value of Zr₆₅Al_{7.5}Ni₁₀Cu_{17.5}

Table 4.3. MGs of various alloy systems and the ΔT_F values for TPFAs comparison.

4.5. Processing temperature map drawing

In this study, an extended analysis of the Kissinger method was used to obtain the CHT curves. [125] Generally, the peak temperature is utilized for Kissinger method, but the crystallization onset temperature, T_x , [126] and T_g [127–128] can be used to replace the peak temperature. The heating rate dependence of the onset temperature of crystallization and glass transition of glassy alloys under the continuous heating treatment can be defined as follow: [129–130]

$$\ln (\beta / (T_x^2)) = (-E) / (R * T_x) + C \quad (1)$$

where T_x can be replaced by T_g , β is the heating rate, E is the activation energy for crystallization or glass transition, R is the gas constant and C is a constant. $\ln (\beta / T_x^2)$ has linear correlation with $1 / T_x$, also with constants of $-E / R$ and C . [127–128] The values of constants can be calculated by the linear fitting with the equation (1). CHT curves of T_x and T_g depending on heating rate can be calculated by the equation (1) with the estimation of onset time by the given heating rate, and the values of slope ($- E / R$) and intercept (C).

$Zr_{76}Ni_{24}$ alloy is a typical marginal MG with narrow ΔT_x , $Zr_{70}Cu_{30}$ alloy represents a particularly wide ΔT_x among Zr-based binary MGs, and $Zr_{70}Cu_{16}Ni_4Co_4Al_6$ alloy is an MG with a wide ΔT_x

developed in this study. **Fig. 4.8. (a–c)** shows CHT curves of T_g and T_x calculated by utilizing conventional DSC (10 K/s or less) and Flash–DSC (10^2 to 10^4 K/s) to identify the heating rate dependency of TPF of each composition. It is known that the closer the melting temperature with the T_x , the better the TPFA, [85] and it is expected that $Zr_{70}Cu_{16}Ni_4Co_4Al_6$ will have more advantages for TPF than the other two binary MGs. The fitted CHT curves estimated through equation (1) fit well with the data measured through conventional DSC and Flash–DSC measurements, and the region between T_x and T_g curves corresponds to a thermoforming window. **Fig. 4.8 (d)** exhibits a comparison of the thermoforming windows of the three compositions. $Zr_{70}Cu_{16}Ni_4Co_4Al_6$ alloy has a higher T_g of about 30 to 40 K than $Zr_{76}Ni_{24}$ alloy, but the thermoforming window is about 60 to 200 K wider, making it more appropriate for TPF process. Besides, this result represents that the range of the ΔT_x differs by more than 100 K even in the same alloy composition according to the heating rate. As shown in the results, processes condition such as forming temperature and speed can be optimized through the definition of accurate CHT curves. In previous studies, many investigations have been performed on the conventional thermoforming window with a slow heating rate of 10 K/s or less, and in the case of $Zr_{76}Ni_{24}$ alloys with narrow ΔT_x , TPF is considered not easy to be applied due to low crystallization resistance. However, under an ultra–fast heating rate of 10^2 K/s or higher, TPF is considered to be applied with a wide ΔT_x of 100 to 150 K even in a marginal MG such as $Zr_{76}Ni_{24}$ alloys,

and $Zr_{70}Cu_{16}Ni_4Co_4Al_6$ alloys exhibits a very wide ΔT_x of 250 to 350 K, so it is expected that stable TPF process is possible even when considering external factors, such as high pressure and fast strain rate.

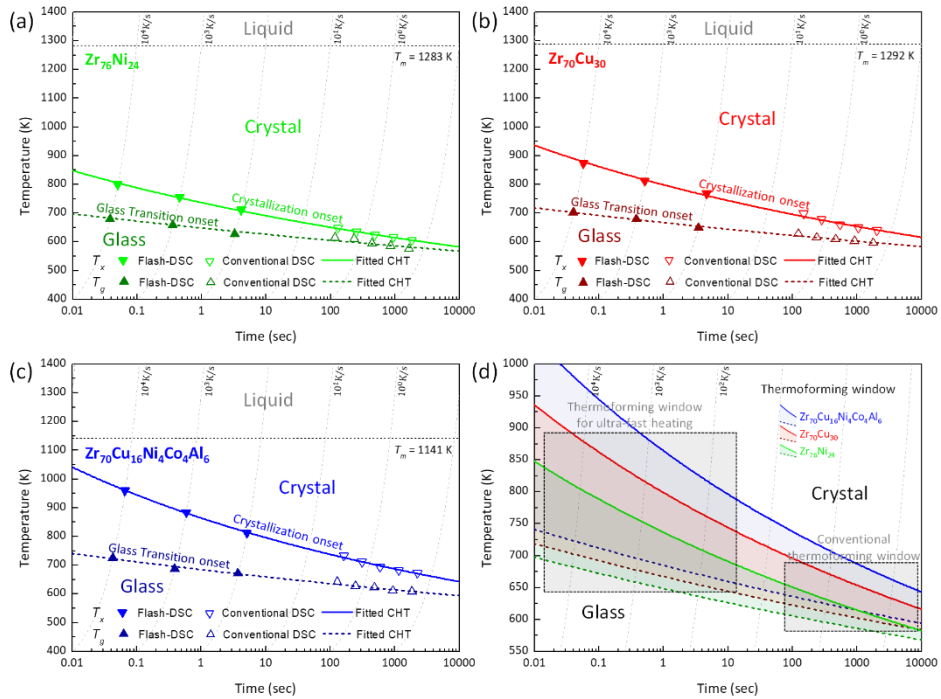


Fig. 4.8. CHT curves and thermoforming windows of the 3 representative alloys developed in this study at various heating rates between 10^{-1} and 10^4 K/s, measured by Flash-DSC. The values of T_g , T_x and the fitted CHT curves for (a) $Zr_{76}Ni_{24}$, (b) $Zr_{70}Cu_{30}$, and (c) $Zr_{70}Cu_{16}Ni_4Co_4Al_6$ alloys. (d) Comparison of temperature–time thermoforming windows between T_g and T_x in CHT curves.

With regard to that $Zr_{70}Cu_{16}Ni_4Co_4Al_6$ alloy exhibits the lowest T_g among the multi-component Be-free Zr-based MGs due to the high Zr content, the TPFA is considered to be relatively excellent. The tendency predicted from ΔT_F can be different in TPF processes performed under non-NVF conditions such as complex geometry, high strain rate, or low temperature. In such a case, the TPFA can be better evaluated by the $S (= m * (T_x - T_g) / (T_1 - T_g))$ parameter. [84] As shown in **Fig. 4.8. (c)**, when the heating rate increases, TPFA can be rapidly improved with an increase in $(T_x - T_g)$ and a decrease in $(T_1 - T_g)$. Besides, the position of the thermoforming window greatly changes according to the heating rate. **Fig. 4.9.** exhibits the comparison of the thermoforming windows between conventional plastics and $Zr_{70}Cu_{16}Ni_4Co_4Al_6$ MG in consideration of the differences depending on the heating rate. The TPFA of engineering plastics is not considered because it could not be evaluated with MG using with the same factor. Instead, the general T_g value of each representative plastics was plotted to determine the criteria for whether related TPF processes and facilities for engineering plastics can be applied to the Zr-based MG developed in this study. The longitudinal solid lines represent the value T_g of each plastic. The blue open triangle represents the TPFA parameter, S , according to the heating rate, T_g and T_x values of $Zr_{70}Cu_{16}Ni_4Co_4Al_6$ MG. A thermoforming window capable for TPF is found in the temperature region between T_g and T_x . If the heating rate is under or equal to about 10^2 K/s, the MG has a lower T_g value than T_g of

conventional PBI or PI, so it is considered that there is sufficiently potential to utilize the TPF process and facilities of plastics for MG. Furthermore, although the T_g of PBI is 683 K, the actual forming process is conducted at a temperature about tens of degrees higher, so it is estimated that the process can be applied to $Zr_{70}Cu_{16}Ni_4Co_4Al_6$ MG even at a heating rate of more than 10^3 K/s. The faster the heating rate, the higher the forming temperature, simultaneously the S parameter increases, and thus the TPFA is improved. Therefore, the micro-to-nano scale TPF process, to which a fast heating rate can be easily applied, is suitable for MG.

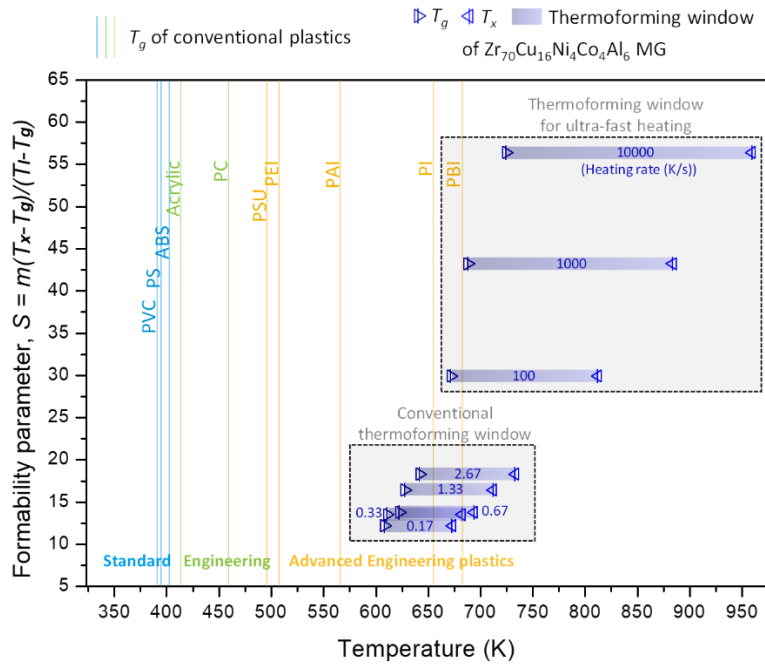


Fig. 4.9. The range of thermoforming window and TPF parameter, $S = (T_x - T_g) / (T_1 - T_g)$, of $Zr_{70}Cu_{14}Ni_4Co_4Al_6$ MG compared to T_g of conventional engineering plastics. The faster the heating rate, the wider the thermoforming temperature range and the better the TPF.

In this work, we found the Zr-based alloy system with the optimal properties for commercialization by applying the TPF process and facilities for conventional engineering plastics among all MG systems developed so far. The lowest achievable T_g in Zr-based MG is fundamentally determined by the Zr content which is related to the high-temperature stability of the beta-Zr phase. The alloy

composition of $Zr_{70}Cu_{16}Ni_4Co_4Al_6$ with the low T_g of 625 K, large thermoforming window, so that excellent TPFA in Zr-based MG was systematically designed. Also, the thermoforming window and TPFA according to the various heating rate were investigated using Flash-DSC. Consequently, it is concluded that the developed MG in this study has sufficient potential to be applied with the processes and facilities of advanced engineering plastics such as PBI and PI. Recently, PI is widely used as applications in the form of a micro-to-nano scale film or fiber, such as medical tubing and coating, insulation layer for MEMS. [131–134] It is expected that the TPF process for such a micro-to-nano sized product is appropriate for the applications of MG considering the GFA, mechanical properties, and heating rate of TPFA. Besides, a TPF facility performed in a vacuum environment is basically suitable for application to MG without any modification. This study is expected to not only contribute to the commercialization of MG by saving the initial investment cost in the process, but also suggest a new possibility that even the marginal MG can exhibit enough thermoforming window to be applied with TPF at a fast heating rate of 10^2 K/s or higher.

Chapter 5.

Development of Zr-based bulk metallic glasses suitable for near-net-shape manufacturing

5.1. Process efficiency in net-shape manufacturing

BMGs have been attracting considerable attention as a high value-added structural material due to their excellent strength and wide elastic limit. [135–138] However, due to low fracture toughness and high hardness, post-treatment such as cutting and milling is very difficult. [137, 139–142] BMGs have the unique benefit of enabling TPF compared to crystalline alloys because they can be processed in a super-cooled liquid state. [142] As the final target shape becomes more complex, the time and pressure required during processing increase, oxidation occurs easily, and there is a risk of degradation of mechanical properties because of relaxation and partial crystallization. [142–143] Therefore, studies about commercializing of BMG for a structural material through near-net-shape casting methods, such as die-casting, suction casting, and injection casting, have been actively investigated. [142–148] This near-net-shape manufacturing for the BMGs has a benefit in low

cost of processing and post-treatment, and maintenance of mechanical properties. [145, 148] Particularly, recent researches has been studied to successfully produce flex spline, a component of a harmonic drive gear with a very complex shape including micro-sized teeth, through suction casting with Zr-based BMG. [144] Structural components with high processing costs and high added value, such as flex spline, are predicted to be in high demand in various industrial fields such as robots, medical care, and automobiles. [149] Thus, near-net-shape manufacturing has significant potential to commercialize BMG in various future-oriented fields.

BMGs suitable for near-net-shape manufacturing should have the following properties: (1) GFA to minimize the possibility of crystalline phase formation under various casting conditions, (2) high mechanical property, such as hardness, or strength, to improve the mechanical stability and extend the life span, and (3) superior fluidity to minimize casting defects and enhance the dimensional accuracy of final products with complex shapes. However, BMG is unfavorable for the near-net-shape casting because it has higher viscosity and surface tension in a molten liquid state compared to crystalline alloys [150–153], although BMG exhibits extremely large undercooling. Specifically, the higher the GFA, the higher the liquid viscosity and the lower the fluidity. Therefore, overcoming the GFA and fluidity trade-off is one of the important issues to fabricate commercial BMG products with complex shapes.

Zr-based BMGs, which are commonly for commercialization, exhibit excellent GFA as well as high mechanical property, such as strength and hardness, and also have relatively outstanding oxidation resistance. In particular, a representative BMG alloy composition, which does not contain the harmful element such as Be, is Vitreloy 106 (Vit-106) developed by Liquidmetal Technology. [154] In this study, we suggest a methodology for developing BMG for near-net-shape manufacturing that has excellent GFA, hardness, and further improved fluidity. Consequently, the novel alloy compositions are designed based on compositional tuning and minor element addition in Vit-106 to manufacture BMG with further desired properties for near-net-shape casting. Besides, the fluidity of developed BMG is evaluated by measuring the flow length through the suction casting method, which has been used to produce the recently reported harmonic drive precision gear. [144]

5.2. Design of quaternary and quinary bulk metallic glass with low T_L

Fig. 5.1. (a) exhibits the liquidus projection of ZrCuNi ternary systems and 10 at. % Al plane of ZrCuNiAl quaternary phase diagram. The modification of Vit-106 alloy (Nb excluded, $Zr_{60.4}Cu_{16.3}Ni_{13.3}Al_{10}$) and $Zr_{60-x}Cu_{16+2x}Ni_{14-x}Al_{10}$ alloy compositions ($x = 0, 2, 4, 6, 8$ at. %, abbreviated into Zr60, Zr58, Zr56, Zr54, and Zr52, respectively) designed around the ternary eutectic point of the ZrCuNi liquidus projection are plotted on the 10 at. % Al plane in ZrCuNiAl quaternary phase diagram. To improve GFA, hardness, and fluidity by finely tuning the alloy composition based on Vit-106, the alloys were designed in a direction expected to have a low liquidus temperature (T_L) by having a ternary eutectic point. In particular, Zr56 is expected as an alloy composition the closest to the ternary eutectic point and to have the lowest T_L . **Fig. 5.1. (b)** exhibits the glass-forming region according to the cooling rate, and a pseudo-binary phase diagram with Zr56 as the eutectic point, Zr60 and Zr58 as hypoeutectic composition, and Zr54 and Zr52 as hypereutectic composition. Although it is arbitrarily shown to have a lower T_L line in hypoeutectic composition, the practical trend needs to be established through experimental results. The growth rate of the crystalline phase is slower near the glass transition temperature on the side with a higher T_L line. [155–157] Thus, the better GFA might

be acquired in the side of hypereutectic compositions where the phase diagram shows a steeper T_L line as **Fig. 5.1. (b)**. Therefore, the eutectic composition where T_L is the lowest, or a hypereutectic composition near eutectic where GFA is excellent can be a potentially suitable composition for near-net-shape casting. Specifically, if the T_L is low, the energy required for melting is low, and the life span of the casting mold and apparatus can be extended, and higher fluidity can be secured under the same temperature condition. Therefore, we investigated the alloy composition with the lowest T_L via compositional tuning in the ZrCuNiAl quaternary alloy system and evaluate the GFA. Besides, Nb and Ag, which are widely known as minor alloying elements in Zr-based BMGs, were added to improve fluidity as well as hardness without degradation of high GFA.

Fig. 5.2. (a) exhibits the XRD patterns obtained by measuring the cross-sections of Vit-106 and $Zr_{60-x}Cu_{16+2x}Ni_{14-x}Al_{10}$ ($x = 0, 2, 4, 6, 8$ at. %) BMGs manufactured by suction casting in the form of a 6 mm diameter rod. All six samples have a typical amorphous phase and exhibit excellent GFA with a maximum thickness (Z_{max}) of 6 mm or more. **Fig. 5.2. (b)** exhibits the heat flow curves measured by DSC, including the characteristic temperatures of metallic glass such as T_g , T_x , and T_L . **Fig. 5.2. (c, d)** represent the changes in T_g , T_x , and T_L measured from the heat flow curves according to the Zr content. T_g and T_x show a constant variation tendency to gradually increase with decrease of Zr content, but in the case of T_L , Zr56 exhibits the lowest value and it is tended to exhibit higher T_L in the hypereutectic of Zr54 and Zr52 than in the hypoeutectic of Zr58 and Zr60. The T_L -Zr content plot represents a similar shape to the T_L line plotted in the schematic pseudo-binary phase diagram in **Fig. 5.1. (b)**. As a result, it is considered that the Zr56 is the composition close to the ZrCuNiAl eutectic composition and represents the lowest T_L . Consequently, Zr56 alloy exhibits higher T_g and T_x values, lower T_L and wider super-cooled liquid region compared to Vit-106.

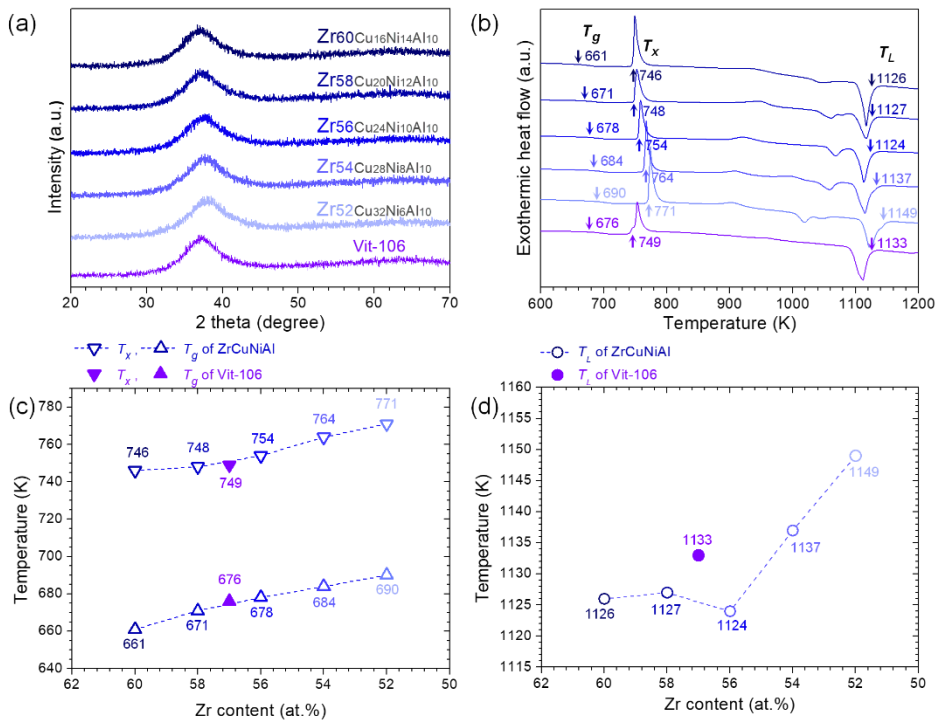


Fig. 5.2. Phase analysis and thermal analysis of the Vit-106 and Zr_{60-x}Cu_{16+2x}Ni_{14-x}Al₁₀ ($x = 0, 2, 4, 6, 8$ at. %) BMGs. **(a)** X-ray diffraction patterns of the as-cast rod samples with 6 mm in diameter. **(b)** Heat flow curves showing characteristic temperatures of MG (T_g , T_x , and T_L). **(c)** Changes in T_g and T_x according to the Zr content. **(d)** Change in T_L according to the Zr content.

Alloy design is further conducted by adding Nb and Ag elements to the ZrCuNiAl BMGs developed in this study, which are considered to improve GFA and mechanical properties of Zr-based BMGs. First, Nb element can improve the GFA of Zr-based BMG, but because it

has been reported to play a role in increasing characteristic temperatures of metallic glass, [158] so that, only a small amount of 3 at. % Nb is added. Studies have been investigated that when Ag is added 5 at. % by substituting Zr in Zr-based BMG, GFA is improved, [159] and when 8 at. % of Ag is added, T_L is significantly reduced. [160] Thus, in this study, 8 at. % of Ag was added to mainly reduce T_L . **Fig. 5.3. (a)** exhibits the XRD patterns obtained by measuring the cross-sections of BMGs with the compositions of $(Zr_{60-x}Cu_{16+2x}Ni_{14-x}Al_{10})_{97}Nb_3$ ($x = 0, 2, 4, 6, 8$ at. %) and $Zr_{54-x}Cu_{16+2x}Ni_{14-x}Al_8Ag_8$ ($x = 0, 4, 8$ at. %), produced by suction casting in the form of 6 mm diameter rods. $Zr_{54}Cu_{16}Ni_{14}Al_8Ag_8$ sample shows a metallic glass matrix composite structure including Zr_2Ni crystalline phase. However, other samples exhibit fully amorphous structure, indicating that they have an excellent GFA with a Z_{max} of 6 mm or more. **Fig. 5.3. (b)** shows the heat flow curves obtained by constant heating rate each BMG sample to a temperature above T_L . **Fig. 5.3. (c, d)** exhibit the changes in T_g , T_x , and T_L depending on the Zr content. The Nb-added ZrCuNiAlNb BMGs have a similar T_g and high T_x and T_L compared to the ZrCuNiAl BMGs. The relatively wider super-cooled liquid region can be more beneficial for TPF, but higher T_L and T_x may help in lower fluidity at the same processing temperature, which is unfavorable for near-net-shape manufacturing by suction casting. Meanwhile, the Ag-added ZrCuNiAlAg BMGs exhibit lower T_x , T_g , and T_L values than the ZrCuNiAl BMGs. Compared with Vit-106 alloy, the ZrCuNiAlNb BMGs show higher T_L , and the ZrCuNiAlAg BMGs

mostly show lower T_L . It can be shown that the minor addition of Ag with substituting Zr element is very efficient in lowering the T_L . In particular, $Zr_{50}Cu_{24}Ni_{10}Al_8Ag_8$ BMG shows the lowest T_L value of 1117 K among the developed BMGs. In the next section, we discuss more detail how to design BMGs appropriate for manufacturing through near-net-shape casting with enhanced the GFA, hardness, and fluidity of the developed BMGs.

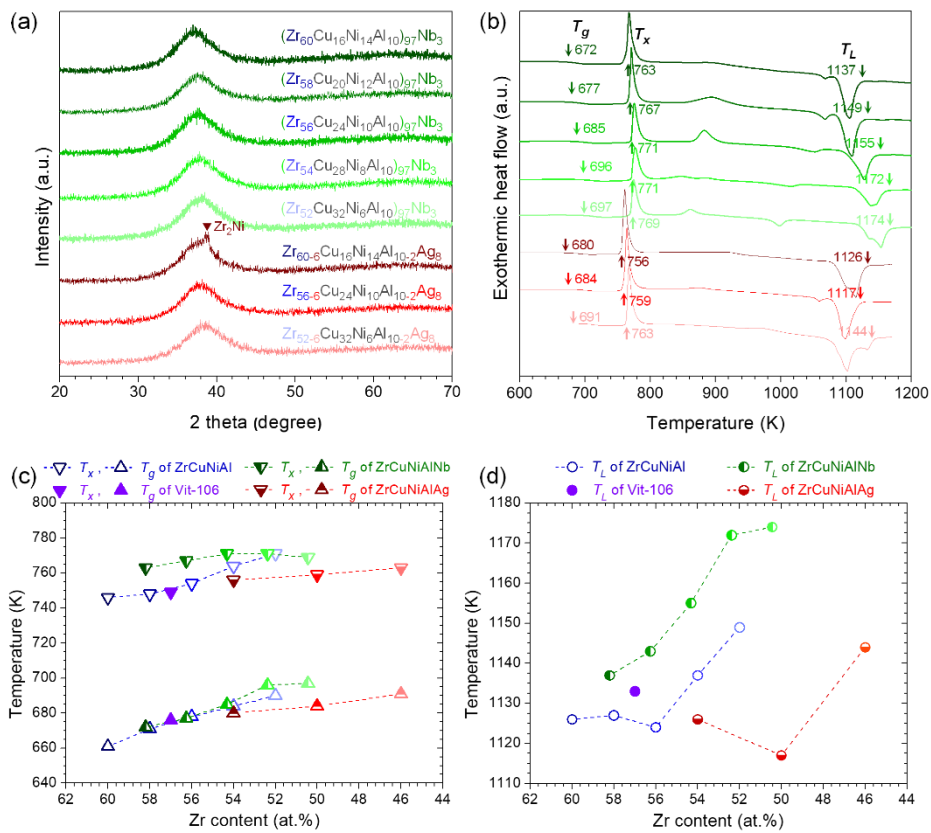


Fig. 5.3. Phase analysis and thermal analysis of the $(\text{Zr}_{60-x}\text{Cu}_{16+2x}\text{Ni}_{14-x}\text{Al}_{10})_{97}\text{Nb}_3$ ($x = 0, 2, 4, 6, 8$ at. %), and $\text{Zr}_{54-x}\text{Cu}_{16+2x}\text{Ni}_{14-x}\text{Al}_8\text{Ag}_8$ ($x = 0, 4, 8$ at. %) BMGs. **(a)** X-ray diffraction patterns of the as-cast rod samples with 6 mm in diameter. **(b)** Heat flow curves showing characteristic temperatures of MG (T_g , T_x , and T_L). **(c)** Changes in T_g and T_x according to the Zr content. **(d)** Change in T_L according to the Zr content.

5.3. Hardness– T_g –Zr content correlation

Previous studies have been reported that solvent element builds the weakest link in glassy structures to dominantly determine elastic modulus, yield strength, hardness, and T_g . [161–163] In the developed Zr-based BMGs, it can be confirmed that Zr content serves as a solvent element. **Fig. 5.4.** exhibits the Vickers hardness test results of the developed BMGs in this study as a 3-dimensional (T_g) – (Vickers hardness) – (Zr content) plot. The fitting results of XY, YZ, and XZ projections exhibit that all three factors have a linear correlation with each other. Therefore, regardless of the content of the additional elements Nb and Ag or the constituent elements of Cu, Ni, and Al, it was considered that Zr contents play an important role as a solvent element forming weak bonding, and other elements do not highly affect hardness and T_g . Because Zr content is a dominant factor that affects mechanical properties, it is important to decrease Zr content in order to improve hardness. When adding an Ag alloying element to Zr-based BMG, it has been investigated that a method of substituting Zr with Ag is desirable for excellent GFA, [159–160] so the addition of Ag element is beneficial for designing BMG with low Zr content and relatively high hardness. Among the BMGs developed in this study, the BMGs containing Ag content exhibit lower Zr content, indicating relatively high hardness.

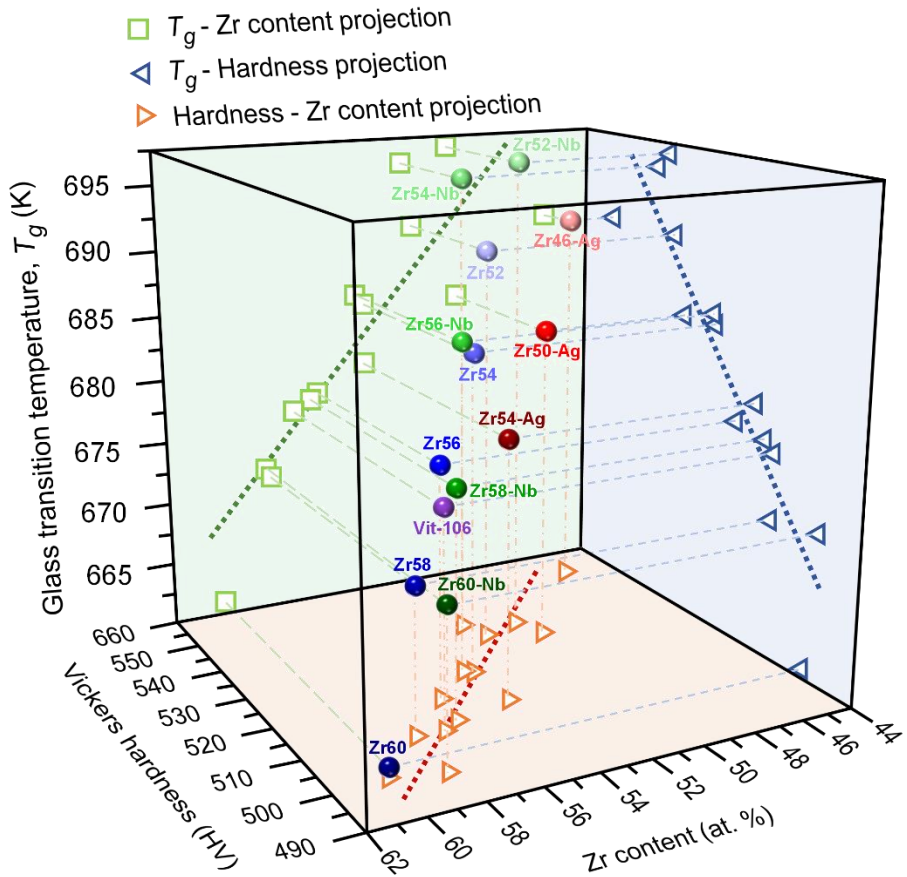


Fig. 5.4. 3-dimensional plot of (T_g)–(Vickers hardness)–(Zr content) of the Zr-based BMGs developed in this study. Three projections (T_g – Zr content / T_g – Hardness / Hardness – Zr content) and their linear fitted lines are arranged on each axial plane.

5.4. GFA evaluation

In order to prevent degradation of BMG properties due to partial crystallization or relaxation, it is essential to design BMG that secures excellent GFA. The critical casting thickness, Z_{\max} , which is directly measured by manufacturing samples of various sizes, can be utilized as a direct indicator of GFA. However, for faster and more efficient BMG-forming alloy development, several GFA evaluation parameters have been suggested that can indirectly estimate GFA using characteristic temperatures. [164–169] Particular, the recently proposed epsilon parameter (ϵ) can effectively predicts Z_{\max} regardless of the alloy system. In this study, the GFA of the developed Zr-based BMG is estimated by calculating ϵ evaluation parameter. A higher ϵ value can be supposed to indicate a higher GFA, and the correlation between ϵ and the characteristic transformation temperatures and Z_{\max} value is as follows [168]:

$$\epsilon = (\Delta T_m + T_x + \Delta T_x) / T_m^{\text{mix}} \quad (1)$$

where $T_m^{\text{mix}} = \sum_1^n n_i * T_m^i$ with n_i and T_m^i being the mole fraction and the melting temperature of i^{th} element and $\Delta T_m = T_m^{\text{mix}} - T_L$,

$$Z_{\max} = 1.48 * 10^{-5} \exp(16.1 \epsilon) \quad (2)$$

Fig. 5.5. (a) exhibits the T_L and ϵ values depending on the Zr content. In all alloy groups of ZrCuNiAl, ZrCuNiAlNb, and

ZrCuNiAlAg, the lower the T_L , the higher the ε value tends to be. It can be considered that the composition with the lowest T_L is close to the eutectic point in each group and represent the best GFA. **Fig. 5.5. (b)** exhibits the $Z_{\max}-\varepsilon$ plots of the Vit-106, 3 selected compositions of each ZrCuNiAl, ZrCuNiAlNb, and ZrCuNiAlAg alloy system with lowest T_L and highest ε developed in this and other previously reported BMGs of various alloy systems. [168] Z_{\max} of the four compositions were estimated by substituting the calculated ε value of the measured characteristic transformation temperatures into Equation (2). The estimated Z_{\max} values are well plotted on the line representing Equation (2) of **Fig. 5.5. (b)**, and the four compositions can be estimated to have a GFA of about 9 mm or more. It can be assumed that there is no significant difference in GFA among the four compositions. Therefore, it is expected that excellent GFA can be obtained in a significantly wide composition range around the $Zr_{56}Cu_{24}Ni_{10}Al_{10}$ composition which is close to the eutectic composition in the ZrCuNiAl quaternary system, even when Nb and Ag elements are added. In the next section, in order to determine alloy composition appropriate for near-net-shape casting, the fluidity is evaluated compared to conventional Vit-106 with the developed BMGs having the lowest T_L of each alloy system.

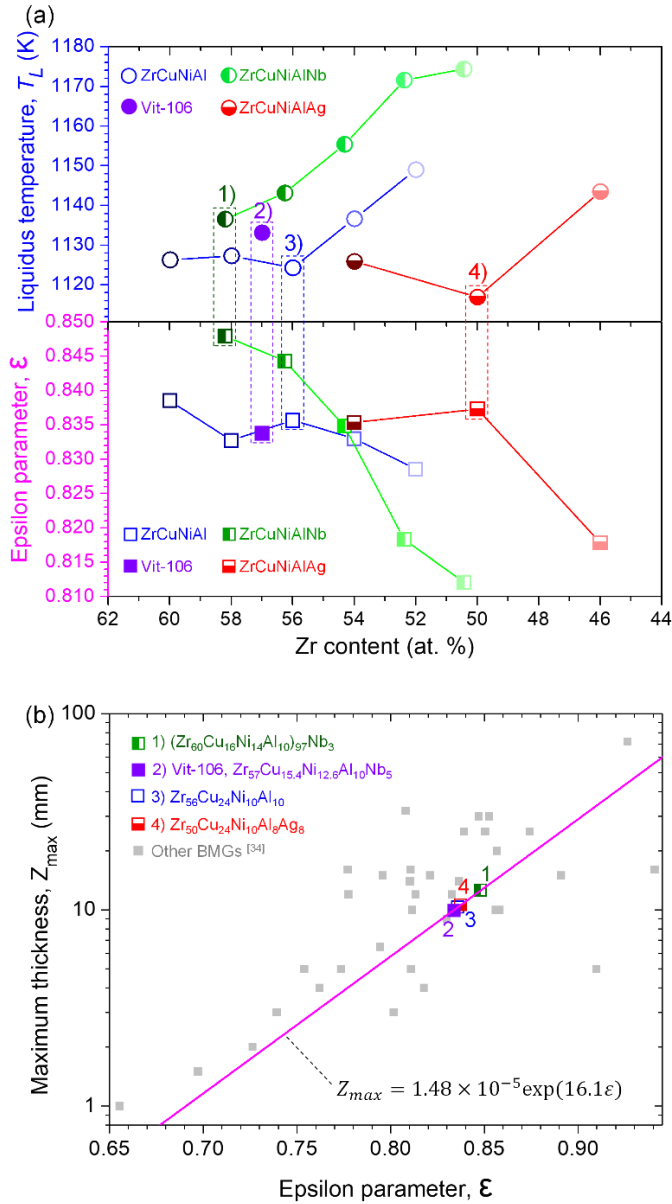


Fig. 5.5. (a) T_L – Zr content, and ϵ – Zr content plots of the Zr-based BMGs developed in this study. (b) Z_{max} – ϵ plots of the Vit-106, three selected alloys with lowest T_L and highest ϵ for each alloy system, ZrCuNiAl, ZrCuNiAlNb, and ZrCuNiAlAg, of **Fig. 5.5.** (a), and other previously reported BMGs of various alloy systems.

5.5. Fluidity test

Because there are differences in pressure, cooling, heating, and contact conditions for the near-net-shape manufacturing, the fluidity evaluation criteria are depending on manufacturing methods such as die casting, suction casting, and injection casting. In this study, the fluidity of BMGs is evaluated through the suction casting method, which is recently reported case of successfully producing the flex spline of precision gear with BMG. [144] The fluidity is quantitatively evaluated by comparing the flow through suction casting using a 1 mm diameter water-cooled Cu mold by uniformly controlling the sample weight, heating, cooling, and pressure conditions. Suction casting is not standardized as a method for evaluating the fluidity of alloys, but it is most widely utilized for manufacturing BMGs. Therefore, evaluating the fluidity of BMG by suction casting is very helpful in that it is possible to verify the flow performance of alloy composition under conditions close to the practical production process. **Fig. 5.6. (a)** exhibits a schematic illustration of suction casting equipment for the fluidity test in this study. The inside of the chamber is equivalently under the condition of an Ar atmosphere of 0.5 bar, and arc plasma is applied with a current of 200 A and maintained for 1 minute to melt the. In order to minimize the temperature difference between the samples during melting, the weight of the sample was precisely controlled to $4.0 \pm$

0.1 g, which is quite a small weight for suction casting. As the suction valve opens, the molten sample is drawn into the Cu mold with a pressure of 0.5 bar, and as shown in **Fig. 5.6. (b)**, the flow length is measured from the top of the mold to the bottom tip of the flowed specimen. **Fig. 5.6. (c)** exhibits the average and standard deviation of the flow lengths of Vit-106 and compositions with lowest T_L selected from the alloys of ZrCuNiAl, ZrCuNiAlNb, and ZrCuNiAlAg, measured 5 times each. The inset images shows representative as-cast samples of each alloy. The 1) $(Zr_{60}Cu_{16}Ni_{14}Al_{10})_{97}Nb_3$ has a similar alloy composition and T_L as those of 2) Vit-106, $Zr_{57}Cu_{15.4}Ni_{12.6}Al_{10}Nb_5$, and their flow length also means a similar average value of about 12.5 mm within the error range. On the other hand, 3) $Zr_{56}Cu_{24}Ni_{10}Al_{10}$ and 4) $Zr_{50}Cu_{24}Ni_{10}Al_8Ag_8$ show lower T_L and significantly larger flow length about 17.1 ± 1.6 mm than those of 2) Vit-106 (about 12.2 ± 0.9 mm). In particular, 4) $Zr_{50}Cu_{24}Ni_{10}Al_8Ag_8$ exhibits about a 40 % increase in flow length compared to that of 2) Vit-106, so it is determined to be a suitable composition for near-net-shape processing through suction casting method. According to these results, when Nb is added, T_L have a tendency to increase in Zr-based BMG, so it is not easy to design a BMG with improved fluidity. In the ZrCuNiAl quaternary BMG-forming alloy system, it was possible to decrease the T_L by designing the composition close to the eutectic point and improve the flow length. When T_L reduces by 1 K, the flow length tends to be enhanced by approximately 0.3 mm in the designed Zr-based BMG-forming

alloys. In addition, when Ag element is added by substituting Zr content to ZrCuNiAl BMG having a lower T_L close to the eutectic point, both hardness and flow length can be further improved. Therefore, it can be assumed that the decrease in T_L in Zr-based BMG forming alloys is considered to play a crucial role in improving fluidity.

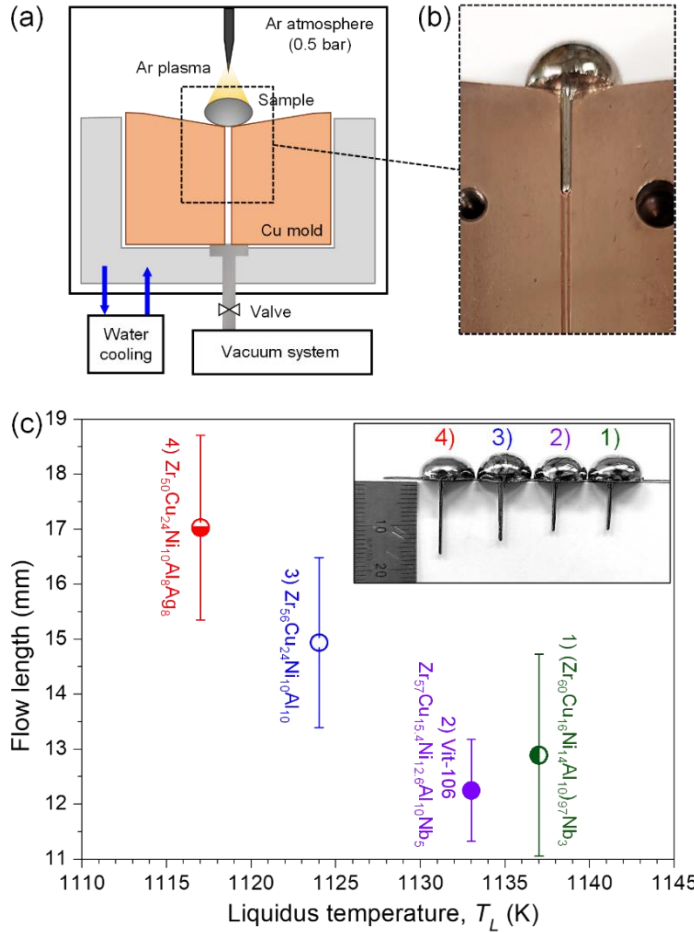


Fig. 5.6. Flow length measurement by suction casting. (a) A schematic illustration of the suction casting equipment for measuring the flow length of BMGs in this study. (b) An image showing that a BMG sample drawn into the 1 mm diameter passage of the Cu mold by suction. (c) Flow length – T_L plot of Vit-106 and the selected alloys with the lowest T_L for the three alloy systems ZrCuNiAl, ZrCuNiAlNb, and ZrCuNiAlAg, respectively. The inset image exhibits the representative samples of each alloy composition for the fluidity test.

In this study, we provide an alloy design methodology that can simultaneously enhance GFA, hardness, and fluidity to be appropriate for near-net-shape manufacturing through suction casting, which can be summarized as follows:

1. Hardness, GFA, and fluidity are sensitively dependent on the alloy composition, especially Zr content, in Zr-based BMG-forming alloys. Because both GFA and fluidity generally complement to each other, in order to improve them simultaneously, the near-eutectic compositions which is high glass-former, Vit-106, carefully investigated by compositional tuning and minor additions.

2. Referring ZrCuNi ternary liquidus projection, it is possible to expect compositions with low T_L close to the eutectic point in the ZrCuNiAl quaternary alloy system.

3. The hardness of Zr-based BMG mainly varies depending on the content of Zr, a solvent element, showing linear correlation rather than the composition of other constituting elements and additional elements, Nb or Ag. In particular, it is efficient to replace Zr with Ag in order to increase hardness while simultaneously obtaining improvement of GFA and reduction of T_L .

4. The $Zr_{50}Cu_{24}Ni_{10}Al_8Ag_8$ BMG developed in this study shows about a 40 % increase in the flow length compared to that of Vit-106 as well as excellent GFA and hardness, which has significant potential to be utilized as high value-added structural materials with complex

shapes through near-net-shape casting.

This study is expected to contribute to the commercialization of BMG as a practical guide to tailor-made alloy design that allows BMG to be applied in the various industrial parts through various near-net-shape casting methods.

Chapter 6.

Conclusion

Due to unique structural characteristics different from the crystalline metal, MGs have excellent mechanical property, such as high strength, large elastic limit of about 2% and high resilience, and exhibits outstanding chemical resistance. Therefore, it is expected to be applied as high-level structural materials. Generally, study on the alloy design for MGs was mainly conducted to find alloy system and composition with better GFA, and in particular, alloy systems containing noble metal element, such as Pt, Au, and Pd, or alloy systems containing toxic element, such as Be. In order to promote the commercialization of MGs, not only considering the cost of alloying elements, but also excluding harmful elements are necessary. Besides, it is necessary to be developed in a way that can be applied to existing manufacturing process, while increasing process efficiency. In this study, the objectives were finding alloys suitable for the net-shape manufacturing, the TPF process which utilizes the intrinsic characteristic temperature of MGs and die-casting which is one of the most common net-shape process used commercially. Prior to practical alloy design of MGs, we first intend to investigate and understand the fundamental background about the correlation between the composition and the property changes in MGs.

MG is one of the simplest glass materials with atoms or atomic clusters like SRO and MRO which interact through metallic bonding. Elastic moduli provide a global and macroscopic view of a stiffness, and reflect both the interatomic bonding energy and connectivity. In particular, the moduli of MGs as readily measurable parameters are the key physical parameter for controlling the main thermodynamic, kinetic, mechanical, and physical properties of MGs. It has been found that the moduli of MGs are inherited from its solvent constituent. When considering the atomic structure of MG, solvent-solvent bonding, where atomic bonding is relatively less stiff, is deformed. Therefore, the moduli of MG are determined by property inheritance of solvent element.

To investigate glass formation and property changes in Zr-based metallic glass, we first produced the ribbon alloys of Zr-TM (= Cu, Ni, Co, Fe) binary systems and measured characteristic temperature. Previous researches have been reported that solvent atoms form the weakest bonding in amorphous structure to mainly determine modulus, strength, and T_g . In this study, it is determined that the tendency of T_g to be determined according to the Zr content is applied to all four alloy systems. It can be thought that MG may have a lower T_g value in a composition with a higher Zr content. Although it is practically impossible, the T_g of pure Zr MG may have a value similar to 517K in trend. Heat flow curves obtained by DSC measurement of the alloy composition with the highest Zr content in each of the four

alloy systems shows that $Zr_{70}Cu_{30}$ MG represents a relatively wide ΔT_x ($= T_x - T_g$) of about 50 K. The other three compositions, $Zr_{76}Ni_{24}$, $Zr_{79}Co_{21}$, $Zr_{77}Fe_{23}$ exhibit typical thermal characteristics of a marginal MG in which crystallization is immediately induced following glass transition during heating.

In this work, we found the Zr-based alloy system which is suitable for being applied the TPF process and facilities for conventional plastics among the other MG systems developed to date. The lowest achievable T_g , $\sim 350^\circ\text{C}$, in Zr-based MG is fundamentally limited by the Zr content because of high stability of the beta-Zr phase. The alloy composition of $Zr_{70}Cu_{16}Ni_4Co_4Al_6$ which has the low T_g of 625 K, large thermoforming window (i.e. over 70K with heating rate 40K/min), and excellent TPFA in Zr-based MG was systematically designed. The thermoforming window, and TPFA depending on the various heating rate were identified by using DSC and Flash-DSC. Accordingly, it can be concluded that the developed MG in this study has sufficient potential to utilize the processes and facilities for advanced engineering plastics such as PBI and PI. These materials are widely used as applications in the form of micro- and nano-scale films or fibers, such as medical tubing and coating, insulation layer for MEMS. Considering the GFA, mechanical properties, and TPFA with heating rate, it is expected that the forming process for such a small-size product is suitable for the developed alloy. This study not only contributes to the commercialization of MG by reducing the

initial investment cost in the process, but also suggests a new possibility that even the marginal MG can have enough thermoforming window to enable TPF at a fast heating rate of 10^2 K/s or higher.

Furthermore, we provided an alloy design methodology that can simultaneously improve GFA, hardness, and fluidity which is suitable for near-net-shape manufacturing through suction casting. Hardness, GFA, and fluidity are sensitively dependent on the alloy composition in Zr-based BMG-forming alloys. Because GFA and fluidity are generally complementary to each other, the near-eutectic compositions around high glass-former, Vit-106, carefully explored by compositional tuning and minor additions. In this study, we utilized ZrCuNi ternary liquidus projection, and it was possible to predict compositions with low T_1 close to the eutectic point in the ZrCuNiAl quaternary alloy system. The hardness of Zr-based BMG linearly depends on the Zr contents, which is a solvent element, rather than the composition of other constituting elements and additional elements. In particular, it was efficient to replace Zr with Ag in order to increase hardness while simultaneously acquiring improvement of GFA and reduction of T_1 . In this study, we developed $Zr_{50}Cu_{24}Ni_{10}Al_8Ag_8$ BMG exhibiting not only excellent GFA and hardness, also about a 40 % increase in flow length compared to that of Vit-106, which is great candidate for high-value structural materials with complex shapes through near-net-shape casting. This study is regarded to contribute to the commercialization of MG

as a practical guide to tailor-made alloy design which allows BMG to be utilized in the various industrial part through various near-net-shape casting methods.

Bibliography

- [1] J. Schroers, Bulk metallic glasses, *Physics Today*, 66, 2, (2013), 32
- [2] E. Ma, Z. Zhang, Reflections from the glass maze, *Nature Materials*, 10, (2011), 0
- [3] W. Buckel, R. Hilsch, Influence of condensation at low temperatures on the electrical resistance and superconduction of various metals, *Zeitschrift für Physik*, 138, (1954), 109
- [4] W. Klement Jun, R.H. Willens, P. Duwez, Non-crystalline structure in solidified gold-silicon alloys, *Nature*, 187, (1960), 869
- [5] D. Turnbull, The 1961 institute of metals division lecture—the liquid state and the liquid-solid transition, *Transaction of the Metallurgical Society of AIME*, 221, (1961), 422
- [6] H.S. Chen, D. Turnbull, Evidence of a glass-liquid transition in a gold-germanium-silicon alloy, *The Journal of Chemical Physics*, 48, (1968), 2560
- [7] H.S. Chen, D. Turnbull, Formation, stability and structure of palladium-silicon based alloy glasses, *Acta Metallurgica*. 17, (1969), 1021
- [8] H.S. Chen, Thermodynamic considerations on the formation

and stability of metallic glasses, *Acta Metallurgica*, 22, (1974), 1505

[9] A.L. Drehman, A.L. Greer, D. Turnbull, Bulk formation of a metallic glass: $\text{Pd}_{40}\text{Ni}_{40}\text{P}_{20}$, *Applied Physics Letters*, 41, (1982), 716

[10] W.H. Kui, A.L. Greer, D. Turnbull, Formation of bulk metallic glass by fluxing, *Applied Physics Letters*, 45, (1984), 615

[11] A. Inoue, T. Zhang, T. Masumoto, Al–La–Ni amorphous alloys with a wide supercooled liquid region, *Materials Transactions, JIM*, 30, (1989), 965

[12] A. Inoue, Stabilization of metallic supercooled liquid and bulk amorphous alloys, *Acta Materialia*, 48, (2000), 279

[13] A. Inoue, T. Nakamura, N. Nishiyama, T. Masumoto, Mg–Cu–Y bulk amorphous alloys with high tensile strength produced by a high pressure die casting method, *Materials Transactions, JIM*, 33, (1992), 937

[14] A. Inoue, High strength bulk amorphous alloys with low critical cooling rates (overview), *Materials Transactions, JIM*, 36, (1995), 866

[15] A. Inoue, T. Zhang, N. Nishiyama, K. Ohba, T. Masumoto, Preparation of 16mm diameter rod of amorphous $\text{Zr}_{65}\text{Al}_{7.5}\text{Ni}_{10}\text{Cu}_{17.5}$ alloy, *Materials Transactions, JIM*, 34, (1993), 1234

[16] A. Peker, W.L. Johnson, A highly processable metallic glass: $\text{Zr}_{41.2}\text{Ti}_{13.8}\text{Cu}_{12.5}\text{Ni}_{10.0}\text{Be}_{22.5}$, *Applied Physics Letters*, 63, (1993),

- [17] Y. Li, S.J. Poon, G.J. Shiflet, J. Xu, D.H. Kim, J.F. Löffler, Formation of bulk metallic glasses and their composites, *MRS Bulletin*, 32, 8, (2007), 624
- [18] C. A. Schuh, T. C. Hufnagel, U. Ramamurty, Mechanical behavior of amorphous alloys, *Acta Materialia*, 55, (2007), 4067
- [19] T. Burgess, M. Ferry, Nanoindentation of metallic glasses, *Materials Today*, 12, (2009), 1
- [20] M.D. Demetriou, M.E. Launey, G. Garrett, J.P. Schramm, D.C. Hofmann, W.L. Johnson, R.O. Ritchie, A damage-tolerant glass, *Nature Materials*. 10, (2011), 123
- [21] Y. H. Liu, G. Wang, R.J. Wang, D.Q. Zhao, M.X. Pan, W.H. Wang, Super Plastic bulk metallic glasses at room temperature, *Science*, 315, (2007), 1385
- [22] J. Schroers, W.L. Johnson, Ductile bulk metallic glass, *Physical Review Letters*, 93, (2004), 25506
- [23] J.J. Lewandowski, W.H. Wang, A.L. Greer, Intrinsic plasticity or brittleness of metallic glasses, *Philosophical Magazine Letters*, 85, (2005), 77
- [24] G. Kumar, S. Prades-Rodel, A. Blatter, J. Schroers, Unusual brittle behavior of Pd-based bulk metallic glass, *Scripta Materialia*, 65, (2011), 585

- [25] R. D. Conner, W.L. Johnson, Shear bands and cracking of metallic glass plates in bending, *Journal of Applied Physics*, 94, (2003), 904
- [26] C. A. Volkert, A. Donohue, F. Spaepen, Effect of sample size on deformation in amorphous metals, *Journal of Applied Physics*, 103, (2008), 083539
- [27] H. Guo, P. F. Yan, Y. B. Wang, J. Tan, Z. F. Zhang, M. L. Sui, E. Ma, Tensile ductility and necking of metallic glass, *Nature Materials*, 6, (2007), 735
- [28] S. Mukherjee, Z. Zhou, J. Schroers, W.L. Johnson, W.K. Rhim, Overheating threshold and its effect on time-temperature-transformation diagrams of zirconium based bulk metallic glasses, *Applied Physics Letters*, 84, (2004), 5010
- [29] B. Lohwongwatana, J. Schroers, W.L. Johnson, Strain rate induced crystallization in bulk metallic glass-forming liquid, *Physical Review Letters*, 96, (2006), 075503
- [30] S. Ding, J. Kong, J. Schroers, Wetting of bulk metallic glass forming liquids on metals and ceramics, *Journal of Applied Physics*, 110, (2011), 043508
- [31] M. Kanik, P. Bordeenithikasem, G. Kumar, E. Kinser, J. Schroers, High quality factor metallic glass cantilevers with tunable mechanical properties, *Applied Physics Letters*, 105, (2014), 131911

- [32] J.J. Gilman, Mechanical behavior of metallic glasses, *Journal of Applied Physics*, 46, (1975), 1625
- [33] J.P. Patterson, D.R.H. Jones, Molding of a metallic glass, *Materials Research Bulletin*, 13, 6, (1978), 583
- [34] K.C. Chan, J. Sort, *Metallic glasses*, Physical Metallurgy Fifth Edition, (2014), 305
- [35] A. Inoue, B. Shen, A. Takeuchi, Developments and applications of bulk glassy alloys in late transition metal base system, *Materials Transactions*, 47, 5, (2006), 1275
- [36] N. Nishiyama, A. Inoue, Glass-forming ability of Pd_{42.5}Cu₃₀Ni_{7.5}P₂₀ alloy with a low critical cooling rate of 0.067 K/s, *Applied Physics Letters*, 80, (2002), 568
- [37] H.T. Zong, M.Z. Ma, L.M. Wang, S.X. Liang, R.P. Liu, Effects of minor addition on glass forming ability: Thermal versus elastic criteria, *Journal of Applied Physics*, 107, (2010), 053515
- [38] A. Peker, W.L. Johnson, A highly processable metallic glass: Zr_{41.2}Ti_{13.8}Cu_{12.5}Ni_{10.0}Be_{22.5}, *Applied Physics Letters*, 63, (1993), 2342
- [39] A.A. Kündig, J.F. Löffler, W.L. Johnson, P.J. Uggowitzer, P. Thiyagarajan, Influence of decomposition on the thermal stability of undercooled Zr–Ti–Cu–Ni–Al alloys, *Scripta Materialia*, 44, (2001), 1269

- [40] Y. Waseda, *The Structure of the Non-crystalline Materials, Liquid and Amorphous Solids*, 2, Mac Graw-Hill, New York, (1980)
- [41] J. D. Bernal, *Geometry of the Structure of Monatomic Liquids*, *Nature*, 185, (1960), 68
- [42] R. Wang, *Short-range structure for amorphous inter transition metal alloys*, *Nature*, 278, (1979), 700
- [43] W.H. Wang, E. Wu, R.J. Wang, S.J. Kennedy, A.J. Studer, *Phase transformation in a bulk amorphous alloy upon crystallization*, *Physical Review B*, 66, (2002), 104205
- [44] D. Holland-Moritz, D.M. Herlach, K. Urban, *Observation of the undercoolability of quasicrystal-forming alloys by electromagnetic levitation*, *Physical review letters*, 71, (1993), 1196
- [45] D.B. Miracle, *A structural model for metallic glasses*, *Nature Materials*, 3, (2004), 697
- [46] D. Ma, A.D. Stoica, X.L. Wang, *Power-law scaling and fractal nature of medium-range order in metallic glasses*, *Nature Materials*, 8, (2009), 30
- [47] A. Hirata, P.F. Guan, T. Fujita, Y. Hirotsu, A. Inoue, A.R. Yavari, T. Sakurai, M.W. Chen, *Direct observation of local atomic order in a metallic glass*, *Nature Materials*, 10, (2011), 28
- [48] Y. Q. Cheng, E. Ma, *Atomic-level structure and structure-property relationship in metallic glasses*, *Progress in Materials*

Science, 56, 4, (2011), 379

[49] X.D. Hui, X. Liu, H. Hou, G.L. Chen, Atomic structures of Zr-based metallic glasses, Science in China Series G: Physics, Mechanics and Astronomy, 51, (2008), 400

[50] J. Dyre, Heirs of liquid treasures, Nature Materials, 3, (2004), 749

[51] V.N. Novikov, A.P. Sokolov, Poisson's ratio and the fragility of glass-forming liquids, Nature 431, (2004), 961

[52] W.H. Wang, Correlations between elastic moduli and properties in bulk metallic glasses, Journal of Applied Physics, 99, (2006), 093506

[53] W.H. Wang, The elastic properties, elastic models and elastic perspectives of metallic glasses. Progress in Materials Science, 57, 3, (2012), 487

[54] Y. Zhang, A.L. Greer, Correlations for predicting plasticity or brittleness of metallic glasses. Journal of Alloys and Compounds, 434-435, 31, 2007, 2-5

[55] W.H. Wang, Properties inheritance in metallic glasses. Journal of Applied Physics, 111, (2012), 123519

[56] Z.Q. Liu, Z.F. Zhang, Universal softening and intrinsic local fluctuations in metallic glasses, Applied Physics Letters, 103, (2013), 181909

- [57] K.W. Park, J.I. Jang, M. Wakeda, Y. Shibutani, J.C. Lee, Atomic packing density and its influence on the properties of Cu–Zr amorphous alloys, *Scripta Materialia*, 57, 2007, 805
- [58] C. Michaelsen, M. Meyer, H.C. Freyhardt, Mössbauer study of Fe-substituted Co-Zr and Cu-Zr metallic glasses, *Journal of applied physics*, 68, (1990), 269
- [59] L.E. Tanner, R. Ray, Metallic glass formation and properties in Zr and Ti alloyed with Be—I the binary Zr–Be and Ti–Be systems, *Acta Metallurgica*, 27, 11, (1979), 1727
- [60] C.Y. Yu, X.J. Liu, J. Lu, G.P. Zheng, C.T. Liu, First–principles prediction and experimental verification of glass–forming ability in Zr–Cu binary metallic glasses, *Scientific Reports*, 3, (2013), 2124
- [61] M. Apreutesei, C. Boissy, N. Mary, M.A.P. Yazdi, A. Billard, P. Steyer, Binary Zr–Ni/Co metallic glass films: Role of the structural state on their durability, *Acta Materialia*, 89, (2015), 305
- [62] D.B. Miracle, D.V Louzguine–Luzgin, L.V. Louzguina–Luzgina, A. Inoue, An assessment of binary metallic glasses: correlations between structure, glass forming ability and stability, *International Materials Reviews*, 55, 4, (2010), 218
- [63] N. Mattern, A. Schöps, U. Kühn, J. Acker, O. Khvostikova, J. Eckert, Structural behavior of $\text{Cu}_x\text{Zr}_{100-x}$ metallic glass ($x = 35-70$), *Journal of Non–Crystalline Solids*, 354, 10–11, (2008), 1054

- [64] D. Ma, A.D. Stoica, X.-L. Wang, Z.P. Lu, B. Clausen, D.W. Brown, Elastic moduli inheritance and the weakest link in bulk metallic glasses, *Physical Review Letters*, 108, (2012), 085501
- [65] M.C. Li, M.Q. Jiang, G. Ding, Z.H. Peng, F. Jiang, L. He, J. Sun, The correlation between weakest configurations and yield strength of Zr-based metallic glasses, *Journal of Non-Crystalline Solids*, 468, 15, (2017), 52
- [66] W.H. Ryu, K.J. Kim, G.H. Yoo, E.S. Park, Alloy design strategy to improve fluidity of Zr-based bulk metallic glass for near-net-shape manufacturing, *Journal of Alloys and Compounds*, 896, (2022), 162680
- [67] J. Schroers, T.M. Hodges, G. Kumar, H. Raman, A.J. Barnes, Q. Pham, T.A. Waniuk, Thermoplastic blow molding of metals, *Materials Today*, 14, 1-2, (2011), 14
- [68] E. Bryn Pitt, G. Kumar, J. Schroers, Temperature dependence of the thermoplastic formability in bulk metallic glasses, *Journal of Applied Physics*, 110, (2011), 043518
- [69] J. Schroers, Processing of bulk metallic glass, *Advanced materials*, 22, 14, (2010), 1566
- [70] A. Inoue, Stabilization of metallic supercooled liquid and bulk amorphous alloys, *Acta materialia*, 48, 1, (2000), 279
- [71] M.F. Ashby, A.L. Greer, Metallic glasses as structural

materials, *Scripta Materialia*, 54, (3), (2006), 321

[72] M. Telford, The case for bulk metallic glass, *Materials today* 7, (3), (2004), 36

[73] A.L. Greer, E. Ma, Bulk metallic glasses: at the cutting edge of metals research, *MRS bulletin*, 32, (8), (2007), 611

[74] W.H. Wang, C. Dong, C.H. Shek, Bulk metallic glasses, *Materials Science and Engineering: R: Reports*, 44, 2–3, (2004), 45

[75] W.L. Johnson, Bulk glass-forming metallic alloys: Science and technology, *MRS bulletin*, 24, 10, (1999), 42

[76] N. Li, W. Chen, L. Liu, Thermoplastic micro-forming of bulk metallic glasses: a review, *Journal of the Minerals, Metals & Materials Society*, 68, (2016), 1246

[77] J. Schroers, Q. Pham, A. Desai, Thermoplastic forming of bulk metallic glass—a technology for MEMS and microstructure fabrication, *Journal of microelectromechanical systems*, 16, 2, (2007) 240

[78] S.M. Song, Y.C. Liao, T.H. Li, C.K. Lee, P.H. Tsai, J.S.C. Jang, J.C. Huang, Thermoplastic deformation behavior of a Fe-based bulk metallic glass within the supercooled liquid region, *Journal of Materials Research and Technology*, 8, 2, (2019), 1907

[79] G. Kumar, A. Desai, J. Schroers, Bulk metallic glass: the smaller the better, *Advanced materials*, 23, 4, (2011), 461

- [80] B. Sarac, G. Kumar, T. Hodges, S. Ding, A. Desai, J. Schroers, Three-dimensional shell fabrication using blow molding of bulk metallic glass, *Journal of Microelectromechanical Systems*, 20, 1, (2010), 28
- [81] H.M. Chiu, G. Kumar, J. Blawdziewicz, J. Schroers, Thermoplastic extrusion of bulk metallic glass, *Scripta Materialia*, 61, 1, (2009), 28
- [82] J. Schroers, Q. Pham, A. Peker, N. Paton, R.V. Curtis, Blow molding of bulk metallic glass, *Scripta Materialia*, 57, 4, (2007), 341
- [83] J. Yi, X.X. Xia, D.Q. Zhao, M.X. Pan, H.Y. Bai, W.H. Wang, Micro-and nanoscale metallic glassy fibers, *Advanced Engineering Materials*, 12, 11, (2010), 1117
- [84] J. Schroers, On the formability of bulk metallic glass in its supercooled liquid state, *Acta Materialia*, 56, 3, (2008), 471
- [85] H.S. Oh, S.Y. Kim, C.W. Ryu, E.S. Park, A criterion of ideal thermoplastic forming ability for metallic glasses, *Scripta Materialia*, 187, (2020), 221
- [86] B. Bochtler, O. Kruse, R. Busch, Thermoplastic forming of amorphous metals, *Journal of Physics: Condensed Matter*, 32, 24, (2020), 244002
- [87] K. Kosiba, Thermoplastic embossing device to probe rheological changes of supercooled metallic liquids during rapid heating, *Review of Scientific Instruments*, 93, 3, (2022), 033901

- [88] G. Kaltenboeck, M.D. Demetriou, S. Roberts, W.L. Johnson, Shaping metallic glasses by electromagnetic pulsing, *Nature Communications*, 7, 1, (2016), 1
- [89] W.L. Johnson, G. Kaltenboeck, M.D. Demetriou, J.P. Schramm, X. Liu, K. Samwer, C.P. Kim, D.C. Hofmann, Beating crystallization in glass-forming metals by millisecond heating and processing, *Science*, 332, 6031, (2011), 828
- [90] G. Kaltenboeck, T. Harris, K. Sun, T. Tran, G. Chang, J.P. Schramm, M.D. Demetriou, W.L. Johnson, Accessing thermoplastic processing windows in metallic glasses using rapid capacitive discharge, *Scientific Reports*, 4, 1, (2014), 1
- [91] J. Throne, Thermoforming, *Applied Plastics Engineering Handbook*, Elsevier, 2011, 333–358.
- [92] T.E. Andres, Polybenzimidazole based materials in automotive tribological applications, *SAE transactions*, (1994), 354–366.
- [93] S.V. Madge, D.V. Louzguine–Luzgin, J.J. Lewandowski, A.L. Greer, Toughness, extrinsic effects and Poisson's ratio of bulk metallic glasses, *Acta Materialia*, 60, 12, (2012), 4800
- [94] T.E. Toolbox, Young's Modulus–Tensile and Yield Strength for common Materials, *Engineering ToolBox United States*, (2003)
- [95] V.R. Sastri, *Plastics in medical devices: properties*,

requirements, and applications, William Andrew, (2021)

[96] E. Baur, T.A. Osswald, N. Rudolph, *Plastics Handbook*, Hanser Publications: Munich, Germany, (2019)

[97] L.W. McKeen, *Film properties of plastics and elastomers*, William Andrew, (2017)

[98] V.R. Sastri, *Engineering thermoplastics: acrylics, polycarbonates, polyurethanes, polyacetals, polyesters, and polyamides*, *Plastics in medical devices*, (2010), 121

[99] Z.Q. Liu, Z.F. Zhang, *Strengthening and toughening metallic glasses: The elastic perspectives and opportunities*, *Journal of Applied Physics*, 115, 16, (2014), 163505

[100] W.H. Wang, *The elastic properties, elastic models and elastic perspectives of metallic glasses*, *Progress in Materials Science*, 57, 3, (2012), 487

[101] F.X. Bai, J.H. Yao, Y.X. Wang, J. Pan, Y. Li, *Crystallization kinetics of an Au-based metallic glass upon ultrafast heating and cooling*, *Scripta Materialia*, 132, (2017), 58

[102] N. Sohrabi, J.E.K. Schawe, J. Jhabvala, J.F. Löffler, R.E. Logé, *Critical crystallization properties of an industrial-grade Zr-based metallic glass used in additive manufacturing*, *Scripta Materialia*, 199, (2021), 113861

[103] N. Li, Y. Chen, M.Q. Jiang, D.J. Li, J.J. He, Y. Wu, L. Liu, A

thermoplastic forming map of a Zr-based bulk metallic glass, *Acta Materialia*, 61, 6, (2013), 1921

[104] T.G. Nieh, J. Wadsworth, C.T. Liu, T. Ohkubo, Y. Hirotsu, Plasticity and structural instability in a bulk metallic glass deformed in the supercooled liquid region, *Acta Materialia*, 49, 15, (2001) 2887

[105] C.A. Schuh, T.C. Hufnagel, U. Ramamurty, Mechanical behavior of amorphous alloys, *Acta Materialia*, 55, 12, (2007), 4067

[106] G. Fan, H.J. Fecht, E.J. Lavernia, Viscous flow of the Pd₄₃Ni₁₀Cu₂₇P₂₀ bulk metallic glass-forming liquid, *Applied physics letters*, 84, 4, (2004), 487

[107] T. Yamasaki, S. Maeda, Y. Yokoyama, D. Okai, T. Fukami, K. HM, A. Inoue, Viscosity measurements of Zr₅₅Cu₃₀Al₁₀Ni₅ and Pd₄₀Cu₃₀Ni₁₀P₂₀ supercooled liquid alloys by using a penetration viscometer, *Materials transactions*, 46, 12, (2005), 2746

[108] D. Xu, G. Duan, W.L. Johnson, Unusual glass-forming ability of bulk amorphous alloys based on ordinary metal copper, *Physical review letters*, 92, 24, (2004), 245504

[109] G. Dalla Fontana, L. Battezzati, Thermodynamic and dynamic fragility in metallic glass-formers, *Acta materialia*, 61, 6, (2013) 2260

[110] Y. Kawamura, T. Nakamura, A. Inoue, Superplasticity in Pd₄₀Ni₄₀P₂₀ metallic glass, *Scripta Materialia*, 39, 3, (1998), 301

- [111] Y. Kawamura, T. Itoi, T. Nakamura, A. Inoue, Superplasticity in Fe-based metallic glass with wide supercooled liquid region, *Materials Science and Engineering: A*, 304, (2001), 735
- [112] H. Tanaka, Relationship among glass-forming ability, fragility, and short-range bond ordering of liquids, *Journal of non-crystalline solids*, 351, 8-9, (2005), 678
- [113] B. Zhang, R.J. Wang, D.Q. Zhao, M.X. Pan, W.H. Wang, Properties of Ce-based bulk metallic glass-forming alloys, *Physical Review B*, 70, 22, (2004), 224208
- [114] H. Kato, Y. Kawamura, A. Inoue, H. Chen, Newtonian to non-Newtonian master flow curves of a bulk glass alloy $\text{Pd}_{40}\text{Ni}_{10}\text{Cu}_{30}\text{P}_{20}$, *Applied Physics Letters*, 73, 25, (1998), 3665
- [115] W. Kim, H.S. Oh, E.S. Park, Manipulation of thermal and mechanical stability by addition of multiple equiatomic rare-earth elements in Al-TM-RE metallic glasses, *Intermetallics*, 91, (2017) 8
- [116] Q.K. Jiang, X.D. Wang, X.P. Nie, G.Q. Zhang, H. Ma, H.J. Fecht, J. Bendnarcik, H. Franz, Y.G. Liu, Q.P. Cao, and J.Z. Jiang, Zr-(Cu, Ag)-Al bulk metallic glasses, *Acta Materialia*, 56, (2008), 1785
- [117] Z.P. Lu, T.T. Goh, Y. Li, S.C. Ng, Glass formation in La-based La-Al-Ni-Cu-(Co) alloys by Bridgman solidification and their glass forming ability, *Acta materialia*, 47, 7, (1999), 2215

- [118] H. Men, D.H. Kim, Fabrication of ternary Mg–Cu–Gd bulk metallic glass with high glass–forming ability under air atmosphere, *Journal of materials research*, 18, 7, (2003), 1502
- [119] B. Gun, K.J. Laws, M. Ferry, Elevated temperature flow behaviour of a Mg–based bulk metallic glass, *Materials Science and Engineering: A*, 471, 1–2, (2007), 130
- [120] W.H. Wang, Correlations between elastic moduli and properties in bulk metallic glasses, *Journal of Applied Physics*, 99, 9, (2006), 093506
- [121] E.S. Park, J.H. Na, D.H. Kim, Correlation between fragility and glass–forming ability/plasticity in metallic glass–forming alloys, *Applied Physics Letters*, 91, 3, (2007), 031907
- [122] J. Kim, S. Shin, C. Lee, Characterization of the gas tungsten arc welded Cu₅₄Ni₆Zr₂₂Ti₁₈ bulk metallic glass weld, *Materials transactions*, 46, 6, (2005), 1440
- [123] A.S. Fetić, G. Remenyi, D. Starešinić, A. Kuršumović, E. Babić, S. Sulejmanović, K. Biljaković, Analysis of the fragility of the Zr₇₇Ni₂₃ metallic glass based on low–temperature heat capacity measurements, *Physical Review B*, 96, 6, (2017), 064201
- [124] D.C. Riegner, *Molecular dynamics simulations of metallic glass formation and structure*, The Ohio State University, 2016.
- [125] D.V. Louzguine, A. Inoue, Evaluation of the thermal stability

of a $\text{Cu}_{60}\text{Hf}_{25}\text{Ti}_{15}$ metallic glass, Applied physics letters, 81, 14, (2002), 2561

[126] J.-H. Kim, J.S. Park, E.S. Park, W.T. Kim, D.H. Kim, Estimation of critical cooling rates for glass formation in bulk metallic glasses through non-isothermal thermal analysis, Metals and Materials International, 11, 1, (2005), 1

[127] R. Svoboda, P. Čičmanec, J. Málek, Kissinger equation versus glass transition phenomenology, Journal of thermal analysis and calorimetry, 114, 1, (2013), 285

[128] G. Ruitenberg, Applying Kissinger analysis to the glass transition peak in amorphous metals, Thermochimica acta, 404, 1–2, (2003), 207

[129] H.E. Kissinger, Variation of peak temperature with heating rate in differential thermal analysis, Journal of Research of the National Bureau of Standards, 57, 4, (1956), 217

[130] K. Mondal, U. Chatterjee, B.S. Murty, Gibb's free energy for the crystallization of glass forming liquids, Applied physics letters, 83, 4, (2003), 671

[131] I. Gouzman, E. Grossman, R. Verker, N. Atar, A. Bolker, N. Eliaz, Advances in polyimide-based materials for space applications, Advanced Materials, 31, 18, (2019), 1807738

[132] J.-S. Jiang, B.-S. Chiou, The effect of polyimide passivation

on the electromigration of Cu multilayer interconnections, *Journal of Materials Science: Materials in Electronics*, 12, 11, (2001), 655

[133] L. Huang, R.S. Dyer, R.J. Lago, A.A. Stolov, J. Li, Mechanical properties of polyimide coated optical fibers at elevated temperatures, *Optical Fibers and Sensors for Medical Diagnostics and Treatment Applications XVI*, SPIE, 2016, 177–184.

[134] Z. Pan, S. Han, J. Wang, S. Qi, G. Tian, D. Wu, Polyimide fabric–reinforced polyimide matrix composites with excellent thermal, mechanical, and dielectric properties, *High Performance Polymers*, 32, 10, (2020), 1085

[135] M.D. Demetriou, M.E. Launey, G. Garrett, J.P. Schramm, D.C. Hofmann, W.L. Johnson, R.O. Ritchie, A damage–tolerant glass, *Nature materials*, 10, (2011), 123

[136] A. Inoue, Bulk amorphous and nanocrystalline alloys with high functional properties, *Materials Science and Engineering: A*, 304 (2001), 1

[137] C.A. Schuh, T.C. Hufnagel, U. Ramamurty, Mechanical behavior of amorphous alloys, *Acta Materialia*, 55, (2007), 4067

[138] W.H. Wang, The elastic properties, elastic models and elastic perspectives of metallic glasses, *Progress in Materials Science*, 57, (2012), 487

[139] C.J. Gilbert, V. Schroeder, R.O. Ritchie, *Fracture and Fatigue*

in a Zr-Based Bulk Metallic Glass, MRS Online Proceedings Library (OPL), 554, (1998).

[140] P.A. Hess, S.J. Poon, G.J. Shiflet, R.H. Dauskardt, Indentation fracture toughness of amorphous steel, Journal of materials research, 20, (2005), 783

[141] J.J. Lewandowski, Effects of annealing and changes in stress state on fracture toughness of bulk metallic glass, Materials Transactions, 42, (2001), 633

[142] J. Schroers, Processing of bulk metallic glass, Advanced materials, 22, (2010), 1566

[143] D.-q. Ma, X.-z. Ma, H.-y. Zhang, M.-z. Ma, X.-y. Zhang, R.-p. Liu, Evaluation of casting fluidity and filling capacity of Zr-based amorphous metal melts, Journal of Iron and Steel Research International, 25, (2018), 1163

[144] D.C. Hofmann, R. Polit-Casillas, S.N. Roberts, J.-P. Borgonia, R.P. Dillon, E. Hilgeman, J. Kolodziejska, L. Montemayor, J.-o. Suh, A. Hoff, Castable bulk metallic glass strain wave gears: towards decreasing the cost of high-performance robotics, Scientific reports, 6, (2016), 1

[145] K.J. Laws, B. Gun, M. Ferry, Effect of die-casting parameters on the production of high quality bulk metallic glass samples, Materials Science and Engineering: A, 425, (2006), 114

- [146] K.J. Laws, B. Gun, M. Ferry, Large-scale production of Ca₆₅Mg₁₅Zn₂₀ bulk metallic glass samples by low-pressure die-casting, *Materials Science and Engineering: A*, 475, (2008), 348
- [147] K.J. Laws, B. Gun, M. Ferry, Influence of casting parameters on the critical casting size of bulk metallic glass, *Metallurgical and Materials Transactions A*, 40, (2009), 2377
- [148] L. Liu, T. Zhang, Z. Liu, C. Yu, X. Dong, L. He, K. Gao, X. Zhu, W. Li, C. Wang, Near-net forming complex shaped Zr-based bulk metallic glasses by high pressure die casting, *Materials*, 11, (2018) 2338
- [149] A. Inoue, N. Nishiyama, New bulk metallic glasses for applications as magnetic-sensing, chemical, and structural materials, *Mrs Bulletin*, 32, (2007), 651
- [150] G. Kumar, J. Blawdziewicz, J. Schroers, Controllable nanoimprinting of metallic glasses: effect of pressure and interfacial properties, *Nanotechnology*, 24, (2013), 105301.
- [151] M. Mohr, R.K. Wunderlich, K. Zweiacker, S. Prades-Rödel, R. Sauguet, A. Blatter, R. Logé, A. Dommann, A. Neels, W.L. Johnson, Surface tension and viscosity of liquid Pd₄₃Cu₂₇Ni₁₀P₂₀ measured in a levitation device under microgravity, *npj Microgravity*, 5, (2019), 1
- [152] S. Mukherjee, W.L. Johnson, W.K. Rhim, Noncontact measurement of high-temperature surface tension and viscosity of bulk metallic glass-forming alloys using the drop oscillation

technique, Applied Physics Letters, 86, (2005), 014104

[153] S. Mukherjee, J. Schroers, Z. Zhou, W.L. Johnson, W.-K. Rhim, Viscosity and specific volume of bulk metallic glass-forming alloys and their correlation with glass forming ability, Acta materialia, 52, (2004), 3689

[154] X.H. Lin, Bulk Glass Formation and Crystallization of Zr-Ti Based Alloys, Ph.D Thesis, California Institute of Technology, 1997, 9227449

[155] D. Ma, H. Tan, D. Wang, Y. Li, E. Ma, Strategy for pinpointing the best glass-forming alloys, Applied Physics Letters, 86, (2005), 191906

[156] H. Tan, Y. Zhang, D. Ma, Y.P. Feng, Y. Li, Optimum glass formation at off-eutectic composition and its relation to skewed eutectic coupled zone in the La based La-Al-(Cu, Ni) pseudo ternary system, Acta Materialia, 51, (2003), 4551

[157] D. Wang, Y. Li, B.B. Sun, M.L. Sui, K. Lu, E. Ma, Bulk metallic glass formation in the binary Cu-Zr system, Applied Physics Letters, 84, (2004), 4029

[158] Y.F. Sun, C.H. Shek, B.C. Wei, W.H. Li, Y.R. Wang, Effect of Nb content on the microstructure and mechanical properties of Zr-Cu-Ni-Al-Nb glass forming alloys, Journal of alloys and compounds, 403, (2005), 239

- [159] W. Zhou, C. Zhang, M. Sheng, J. Hou, Glass forming ability and corrosion resistance of Zr–Cu–Ni–Al–Ag bulk metallic glass, *Metals*, 6, (2016), 230
- [160] W. Zhang, Q. Zhang, C. Qin, A. Inoue, Synthesis and properties of Cu–Zr–Ag–Al glassy alloys with high glass–forming ability, *Materials Science and Engineering: B*, 148, (2008), 92
- [161] M.C. Li, M.Q. Jiang, G. Ding, Z.H. Peng, F. Jiang, L. He, J. Sun, The correlation between weakest configurations and yield strength of Zr–based metallic glasses, *Journal of Non–Crystalline Solids*, 468, (2017), 52
- [162] D. Ma, A.D. Stoica, X.–L. Wang, Z.P. Lu, B. Clausen, D.W. Brown, Elastic moduli inheritance and the weakest link in bulk metallic glasses, *Physical Review Letters*, 108, (2012), 085501
- [163] N. Mattern, A. Schöps, U. Kühn, J. Acker, O. Khvostikova, J. Eckert, Structural behavior of $\text{Cu}_x\text{Zr}_{100-x}$ metallic glass ($x = 35–70$), *Journal of Non–Crystalline Solids*, 354, (2008), 1054
- [164] I.W. Donald, H.A. Davies, Prediction of glass–forming ability for metallic systems, *Journal of Non–Crystalline Solids*, 30, (1978), 77
- [165] A. Hrubý, Evaluation of glass–forming tendency by means of DTA, *Czechoslovak Journal of Physics B*, 22, (1972), 1187
- [166] A. Inoue, High strength bulk amorphous alloys with low

critical cooling rates (overview), *Materials Transactions, JIM*, 36 (1995), 866–875

[167] Z.P. Lu, C.T. Liu, A new glass-forming ability criterion for bulk metallic glasses, *Acta materialia*, 50, (2002), 3501

[168] E.S. Park, C.W. Ryu, W.T. Kim, D.H. Kim, A novel parameter to describe the glass-forming ability of alloys, *Journal of Applied Physics*, 118, (2015), 064902

[169] D. Turnbull, Under what conditions can a glass be formed?, *Contemporary physics*, 10, (1969), 473

Abstract in Korean

Net-shape 공정을 위한 Zr계 비정질 합금의 맞춤형 설계

김경준

서울대학교 공과대학

재료공학부

비정질 합금은 고강도 및 약 2%의 넓은 탄성 한계를 나타내는 등 우수한 기계적 특성을 보이며, 높은 액상 안정성에 의한 뛰어난 주조성 및 열가소성 성형이 가능한 독특한 특성에 의하여 차세대 구조 재료로 주목 받고 있다. 비정질 합금의 상용화를 촉진하기 위해서는 구성 원소의 가격이 고려되어야 하며 Be 등의 유해성 원소가 배제되는 것이 바람직하다. 또한 공정 효율을 높일 수 있는 방향으로 최적화된 합금 조성이 개발될 필요가 있다. 본 연구에서, 우리는 각각 열가소성 성형 공정과 net-shape 공정에 적합한 Zr계 비정질 신합금을 개발했다. 먼저 비정질 합금의 조성과 특성 변화에 관한 상관 관계를 파악하고 그 이론에 대한 기본적인 배경을 조사하고자 했다. 비정질 합금의 탄성 계수는 강성에 대한 거시적인 관점을 제공하며, 이는 원자간 결합 에너지를 반영하는 인자이다. 특히 이는 비정질 합금의 열 특성 및 기계적 특성 등 전반적인 특성과 상관 관계에 있는 필수적인 인자이다. 일반적으로 비정질

합금의 탄성 계수는 원자 결합이 상대적으로 느슨한, 용매 원자 간 결합의 변형에 의해서 결정되는 것으로 간주된다. 따라서 비정질 합금의 특성은 용매 원소의 특성이 유전되는 것으로 알려져 있다.

Zr계 비정질 합금의 특성 변화를 조사하기 위해, Zr과 전이 금속 (= Cu, Ni, Co, Fe) 간 이성분 합금계의 리본 합금을 멜트 스피닝 방식을 통해 제조했다. X선 회절과 고에너지 X선 산란을 통해 비정질 상 형성을 조사했으며, 시차 열 분석법을 통해 비정질 합금의 특성 온도를 측정했다. 본 연구를 통해, 4개의 Zr과 전이 금속 간 이성분 합금계 모두 Zr 함량에 따라 유리 천이 온도 (T_g), 결정화 온도 (T_x) 등의 특성 온도 경향이 결정되는 것을 확인했다. Zr 함량이 높을수록 유리 천이 온도가 더 낮아지는 것으로 고려된다. 순수 Zr 함량 100%의 비정질 합금을 만들 수 있다면, 해당 합금은 약 517 K의 낮은 유리 천이 온도를 가지는 것으로 확인된다. 각 이성분 합금계에서 Zr 함량이 가장 높은 조성들 중 $Zr_{70}Cu_{30}$ 조성만이 약 50 K의 상대적으로 넓은 과냉 액체 영역을 가진다.

비정질 합금의 특성과 조성에 관한 기본적인 이해를 바탕으로, 본 연구진은 기존의플라스틱 열가소성 성형을 위한 공정과 설비에도 적용될 수 있는, 최적의 특성을 가진 새로운 Zr계 합금을 개발했다. 베타 Zr 상의 높은 안정성 때문에 기본적으로 Zr계 비정질 합금에서 유리 천이 온도를 낮추는 합금 설계는 제한된다. 본 연구에서 열가소성 성형이 적용되는 기존 Zr계 비정질 합금에 비해 상대적으로 낮은 625 K의 유리 천이 온도를 가지면서, 동시에 넓은 열가소성 성형 온도 범위, 우수한 열가소성 성형능을 가지는 $Zr_{70}Cu_{16}Ni_4Co_4Al_6$ 합금이 개발되었다. 여러 승온 속도에서의 열가소성 성형 온도 범위나 열가소성 성형능은 DSC와

Flash-DSC를 통해 측정 되었다. 본 연구에서 개발된 비정질 합금은 PBI, PI와 같은 첨단 엔지니어링 플라스틱의 공정과 설비를 활용하여 성형이 가능한 합금이다. 비정질 형성능과 기계적 특성, 승온 속도에 따른 열가소성 성형능을 모두 고려할 때, 개발된 합금은 마이크로- 및 나노-스케일 필름이나 섬유 같은 소형 제품의 성형 공정에 적용 가능할 것으로 예상된다.

또한, 본 연구진은 비정질 형성능, 경도 및 흐름성을 고려함과 동시에 진공 주조법을 통한 net-shape 공정에 적합한 합금 설계 방법론을 제조할 수 있었다. 비정질 형성능, 경도 및 흐름성은 Zr계 벌크 비정질 합금에서 조성과 상관 관계를 가지는 알려져있으며, 이는 본 연구에서 제조된 합금과 보고된 합금들의 특성에 대해 통계적으로 조사함으로써 상관 관계를 파악할 수 있었다. 일반적으로 비정질 형성능과 흐름성은 서로 상충하는 관계에 있는 특성인데, 비정질 형성능이 큰 조성일수록 점도가 높아 흐름성이 감소하기 때문이다. 하지만, 비정질 형성능과 흐름성은 공정 온도 주변의 조성으로 설계함으로써 동시에 해결 가능하다. 본 연구진은 Zr-Cu-Ni 3원계 합금계의 액상 온도 선을 활용하여, Zr-Cu-Ni-Al 4원계 합금 조성 중 공정 온도에 가까운, 낮은 액상 온도를 가지는 합금을 예측했다. 이때, Zr을 Ag로 소량 치환할 경우 경도를 증가시킬 뿐만 아니라 비정질 형성능의 개선과 액상 온도의 감소를 동시에 확보할 수 있었다. 본 연구에서 개발된 $Zr_{50}Cu_{24}Ni_{10}Al_8Ag_8$ 벌크 비정질 합금은 큰 비정질 형성능과 높은 경도를 보일 뿐만 아니라, 상용 Vit-106 합금 대비 40% 가량 증가한 흐름성을 가지는 것으로 확인됐다. 개발된 벌크 비정질 합금은 net-shape 공정을 통해 복잡한 형상으로 제작 가능한, 고부가가치 구조 재료로 활용 가능할 것으로 기대된다.

본 연구는 기존 플라스틱의 열가소성 성형을 위한 공정 및 설비에 적용 가능한, 최적화된 합금 설계 방식 뿐만 아니라 비정질 형성능, 경도 및 흐름성을 동시에 확보하면서 net-shape 공정에 적용 가능한 합금 설계 방식을 제시한다. 본 연구는 열가소성 성형 공정의 초기 투자비용을 절감함으로써 비정질 합금의 상용화를 촉진함을 보여준다. 또한 net-shape 주조 공정을 적용함으로써 벌크 비정질 합금을 다양한 산업 부문에 활용할 수 있는 맞춤형 합금 설계를 제시한다.

핵심 단어 : 비정질 합금, 벌크 비정질 합금, 열가소성 성형, 열가소성 성형 온도, Net-shape 주조 공정, 흐름성

학 번 : 2015 - 20799